NTNU – Trondheim
Norwegian University of
Science and Technology

Lessons from Nature - Surface Characterisation by means of Nanotechnology

Henrik Olerud

Master of Science in Engineering and ICT
Submission date: February 2013
Supervisor: Christian Thaulow, IPM

Norwegian University of Science and Technology
Department of Engineering Design and Materials

Abstract

There is still much to learn from nature. Springtails (*collembola*), a small arthropod that live in soil and decaying material, have through evolution developed extremely effective anti-wetting skin patterns. The hexagonal structure on the cuticle of some species distinguishes them from other anti-wetting surfaces and makes them an interesting study. In this thesis, two different methods of surface characterization were utilized. In the end there was an evaluation on which method that was the best.

Method one consisted of analysing images taken with a Focused Ion Beam (FIB). A dual-FIB was utilized, which consists of both a FIB and a Scanning Electron Microscope (SEM). This made it possible to cut in to the surface structure on a nanoscale. The samples were then tilted, so one could view the cross-section and take SEM images. The images was then analysed and height values of the selected species extracted.

A 3D image was also possible to obtain from the SEM images from the FIB. This was done by powerful image analytic software. The program analysed hundreds of SEM pictures taken only a few nm apart, sliced by the FIB. This produced a 3D image. The method was called "slice and view".

The second method consisted of the use of a nanoindenter. A nanoindenter performed a Nanoindenter-"Atomic Force Measurement" scan, or NI-AFM scan, which produced a 3D image of the surface of the scanned sample. The height data was then relatively easy extracted from the images.

In addition some mechanical properties of the specie *F. quadrioculata* were measured. This was performed by nanoindenting. Nanoindenting consists of performing an indent on the surface and extract data of the forces used and how the material behaved. The data were then analysed and evaluated. The reduced Young's modulus and hardness were the material properties that were extracted.

A total of five different species of springtails were tested with both methods. One deemed unscannable by the NI-AFM, but produced a beautiful 3D image by the "slice and view" method. The resulting four species was evaluated. To conclude, the springtail cuticles with the lowest surface structures, *I. prasis* and *F. quadrioculata*, was best fitted for the NI-AFM scans and hardest to analyse from the images of the cross sections.

The indentation of *F. quadrioculata* confirmed some of the mechanical properties we know. The granules and bridges between the granules are harder than the skin between them. Nanoindentation of soft materials is a field increasing in scope. More material testing of the cuticles of springtails are reccomended.

Sammendrag

Det er fremdeles mye å lære fra naturen. Spretthaler (*collembola*), et lite leddyr som lever i jorda, har gjennom evolusjonen utviklet strukturer i kutikulaen som gjør dem ekstremt vannavstøtende. Enkelte arter har veldig distinkte heksagonale strukturer som skiller spretthalene fra andre vannavstøtende overflater. Dette gjør dem interessante å studere. I denne oppgaven brukte jeg to forskjellige metoder for overflatekarakterisering og gjorde deretter en evaluering av hvilken som egnet seg best.

Metode en innebar analysering av bilder tatt med en Focused Ion Beam (FIB). En dual-FIB ble brukt. Denne inneholdt både en FIB og et Skanning elektronmikroskop (SEM). Dette gjorde det mulig å kutte hull inn i overflatestrukturen med nanometerpresisjon. Prøvene ble tiltet slik at hullet i overflatestrukturen kom på skrå i forhold til SEMen. Resultatet ble bilder av et tverrsnitt av overflatestrukturen. Dette bildet ble så bli analysert, og man kunne blant annet få ut høyden på overflatestrukturene.

Det var også mulig å lage 3D bilder basert på SEM bildene fra FIBen. Dette innebar å ta flere hundre tverrsnittbilder med SEM, bare et par nm fra hverandre. Ved hjelp av kraftig bildeanalyseringsprogramvare utgjorde disse et 3D bilde. Metoden ble kalt ≪slice and view≫.

Metode to innebar bruk av en nanoindenter. Nanoindenteren skannet overflatestrukturene og produserte et 3Dbilde av overflaten. Høydedataene til overflatestrukturene ble dermed relativt lett hentet ut.

I tillegg ble nanoindenteren brukt til å hente ut de mekaniske egenskapene til arten *F. quadrioculata*. En indentering gikk ut på å trykke liten nål ned i overflaten og registrere hvordan materialet oppførte seg. Fra indenteringene fikk man opp grafer som deretter ble analysert. Redusert E-modul og hardhet er materialegenskapene som ble hentet ut.

Totalt ble fem forskjellige arter av spretthaler testet med begge metoder. Det viste seg umulig å avbilde *H. viatica* med nanoindenteren, men et vakkert 3D bilde ble tatt med ≪slice and view≫ metoden. De resterende fire artene ble evaluert. Konklusjonen var at spretthalene med de laveste overflatestrukturene, *I. prasis* og *F. quadrioculata*, lot seg best avbilde i nanoindenteren. Disse var også de som var vanskeligst å analysere basert på bilder av tverrsnitt.

Indenteringen av *F. quadrioculata* bekreftet noen av de materialtekniske egenskapene vi vet om dyret fra før av. Granulene og broene mellom granulene er litt hardere enn huden i mellom. Nanoindentering av myke materialer er et felt økende omfang. Mer testing av de mekaniske egenskapene til spretthaler er anbefalt.

Acknowledgements

This master thesis was produced from fall 2012 to February 2013 at the Norwegian University of Science and Technology (NTNU), Department of Engineering Design and Materials (IPM). Characterization experiments were performed at NTNU Nanolab and the laboratories of IPM at NTNU.

I would like to thank my supervisor Christian Thaulow for giving me the opportunity to access these great instruments and showing great enthusiasm and interest in my findings. A big thank goes as well to my contact person and PhD candidate Håkon Holm Gundersen. He always takes his time to help me with my work and supply me with data from his own research. He has also prepared some of the samples and instructed me in sample preparation. In addition I would like to thank Bjørn Rune Rogne for teaching me to use and understand the FIB and the nanoindenter and Vidar Tonaas Fauske for teaching me to use the integrated FIB software and the corresponding software for scientific visualization and data analysis.

Contents

List of Figures

1. Introduction

Humans have always been astounded by nature. Since the beginning of time, nature has adopted and changed itself to better face new possibilities and challenges. As long as humans have existed we have tried to replicate and improve the designs of nature. Nature has developed processes and materials that function from the macro scale to the nano scale. Properties of the surfaces of biological materials results from a complex interplay between surface morphology and chemical and physical properties [1]. Superhydrophobicity [1], self-cleaning, drag reduction in fluid flow and energy conservation are some of many examples of properties found in nature that are of commercial interest.

There are many plants and animals that utilize their nanostructured surfaces to survive. Figure 1.1 displays some of the most well-known plants and animals that display highly specialized surface structures. One of the most well known and most studied superhydrophobic structure is the Lotus leaf [2]. The self-cleaning properties of the lotus leaf even has its own trademark, the "Lotus Effect". Seen in figure 1.1(a) is a water droplet on the surface a lotus leaf. The droplet is nearly spherical. This indicates that water does not adhere strongly to the lotus leaf. Marmur [3] concluded that metastable states are the key to superhydrophobicity on Lotus leaves. Manhui Sun and Chen [4] explained that the microscopic structure on the lotus leaf consists of papillose epidermal cells covered in self-assembled nanocrystalline wax tubules.

The water strider *Gerris remigis*, seen in figure 1.1(b), has remarkable non-wetting legs that enables it to stand effortlessly and move quickly on water. This is due to the remarkable special hierarchical structure on the legs, which are covered by large numbers of oriented tiny hairs with fine nano grooves [5].

The gecko also has some remarkable abilities, seen in figure 1.1(c). How does it stick to nearly every surface while supporting its own weight? This is due to good adhesion to the surface. Hansen [6] concluded that isolated, the gecko setae are self-cleaning, thus making it better stick to the surface. As a superhydrophobic surface, the gecko is also interesting to examine, as it can clean even when dry [2].

When the grey reef shark, seen in figure 1.1(d), flows through the water, very small individual tooth-like scales, called dermal denticles, work together to reduce the formation of vortices present. This greatly reduces the drag since the water is moving more efficiently over the surface [7].

The eyes of the moth, figure 1.1(e), are anti-reflective to visible light. Bushan [1] states that they consist of hundreds of hexagonally organized nanoscopic pillars which present an

[1] The definition of what makes a surface superhydrophobic will be given in Section 2.2

interesting optical phenomenon. This effect has been known and applied for many years at longer wavelengths, but can also be applied and copied artificially at optical wavelengths. The moth eyes feature on metallic surfaces can have a spectral reflectance which makes them ideal as selective solar absorbers [8].

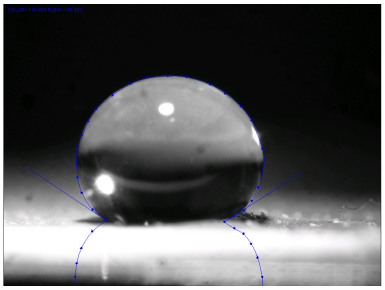

(a) A water droplet on a **lotus leaf** exemplifying high contact angle [9].

(b) **Pond skater** has the ability to walk on water [5].

(c) Close-up of the underside of a **Gecko's** foot as it walks on vertical glass [10].

(d) Grey reef **shark**, as example of sharks that are covered in dermal denticles, reducing drag when they swim [11].

(e) **Moth eyes** are antireflective to visible light [12].

Figure 1.1: Montage of different designs of nature.

Biomimetics is the study of structures on biological systems. This can then be used as a model for design and engineering of new materials. Patankar [13] has produced double (or multiple) roughness structures on pillars to mimic the surface geometrics of self-cleaning surfaces, such as the lotus leaf. Sullivan [14] has replicated the surface structure

of the shark skin. They characterized the dermal denticles of the slow-swimming shark *Scyliorhinus canicula* and successfully produced synthetic sharkskin samples using the real skin as a template. The sub wavelength scale antireflection moth-eye structures in silicon were fabricated by a wafer-scale nano imprint technique [15]. Studies of the moth's eye has for instance led to brighter cellular phone screens and better anti counterfeiting techniques [16].

Thor Christian Hobæl [17] lists some effects that we got from surfaces with superhydrophobic properties. From the lotus leaf one would get self-cleaning surfaces, windows that do not have to be washed. If the water cant stick to the surface, no ice would form either, leading to airplanes that do not have to go through anti-icing. Little corrosion would form on steal or metal surfaces with superhydrophobic properties since water is required for the metal to corrode. As the shark skin, superhydrophobic surfaces would greatly reduce the drag in structures near or in water.

Springtails, *collembola*, a small arthropod, has a special surface structure on its cuticle that has long been known to be water repellent. [18]. When studied in Scanning Electron Microscope (SEM), micron-sized hexagonal patterns are revealed on the cuticles of several species. In combination with a wax layer covering the entire cuticle, these structural features are believed to be the reason for their non-wettable nature. There are great variations among the different species; some have bigger, secondary granules, while on others the surface structures consists of lower primary granules. Some species are covered fully or partially in hair, while others are hairless. [18] [19] [20] [21] The speculation is whether this is to reflect the adaptation to different environments the various species are living in, or heritage, which family the species belong to.

Helbig et al. [22] uncovered how the skin of the springtail is substantially more mechanically stable due to incorporated, flexible bristles and the comb-like alignment of granules. They also performed experiments in order to assess the mechanical properties of the cuticles. The results suggested that the springtail cuticles have a damage resistance that is clearly superior to that of the natural superhydrophobic surfaces found on plants.

The results of previous studies certainly inspire further investigation. Little actual data on the exact size and shape of these sub-micron structures exists. This data would be vital for future biomimetic replication, thus we wish to provide it with this report.

The investigation was based on two different approaches. SEM images of cross section of the cuticle were measured to get real height data of the structures. In addition a nanoindenter was used to perform image scans of the cuticle. This produced 3D images with height data. Nanoindentations were also performed to provide measurements of the mechanical properties of the cuticles.

The outline of the report is as follows. In section 2, we review the most essential wetting and mechanical theory for our cause. Next, in section 3, we present the equipment and methods used to develop the images needed, and how to extract the data from the images. The discussion in section 4 reviews which method that produces the most reliable data. Finally we draw conclusions in section 6 and suggest directions for future research in section 7.

2. Theory

As the structures on the springtail cuticle display a surface with roughness, the effect of such roughness must be understood to explain the superhydrophobicity of the arthropod.

2.1 Tribology

Tribology is the science and engineering of interacting surfaces in relative motion. This includes the study and application of the principles of friction, lubrication and wear. One key function of friction is the roughness of the surface [23]. Surface roughness is a characterization of the surface topography [24].

There are many definitions of what roughness is. Wenzel [25] proposes that roughness modifies wetting characteristics. There is a ratio of the surface areas and it cannot be determined by measurement of surface profiles. In equation (2.1), where relating specific interfacial energies, surface roughness, and the equilibrium contact angle $\boldsymbol{\theta}$, the surface factor r is defined as the ratio of the area of the actual surface to that of a smooth surface having the same geometric shape and dimensions, explained in equation (2.2).

$$r(S_S - S_{SL}) = S_L cos\boldsymbol{\theta} \tag{2.1}$$

$$r = \frac{actual\ surface}{nominal\ surface} \tag{2.2}$$

2.2 Wetting on Rough Surfaces

The general understanding is that the roughness of a surface contributes to its hydrophobicity. How hydrophobic a surface is, depends on the contact angle $\boldsymbol{\theta}$. This is the angle between the liquid-gas interface and the liquid-solid interface when a droplet rest on a solid surface, as seen in figure 2.1(a).

The term hydrophobic is defined as a droplet with $\boldsymbol{\theta} > 90°$, and superhydrophobic is when the $\boldsymbol{\theta}$ exceeds 150° [1]. The contact angle is formed at the end of the droplet, which is called the contact line. Where $\boldsymbol{\theta} = 180°$, a small enough droplet will be spherical, larger ones will be flattened due to gravity [26]. Different theories have been established over the years, as to how a droplet is reacting when in contact with a surface.

2.2.1 Young's Statement

According to Young's statement [27], the contact angle $\boldsymbol{\theta}$ is defined by analysing the forces acting on a fluid droplet resting on a solid surface surrounded by a gas, see figure 2.1(a).

$$\gamma_{SG} = \gamma_{SL} + \gamma_{LG} cos\boldsymbol{\theta} \tag{2.3}$$

In equation (2.3), γ_{SG} is the interfacial tension between the solid and gas, γ_{SL} is the iterfacial tension between the solid and liquid and γ_{LG} is the interfacial tension between the liquid and gas, see figure 2.1(a).

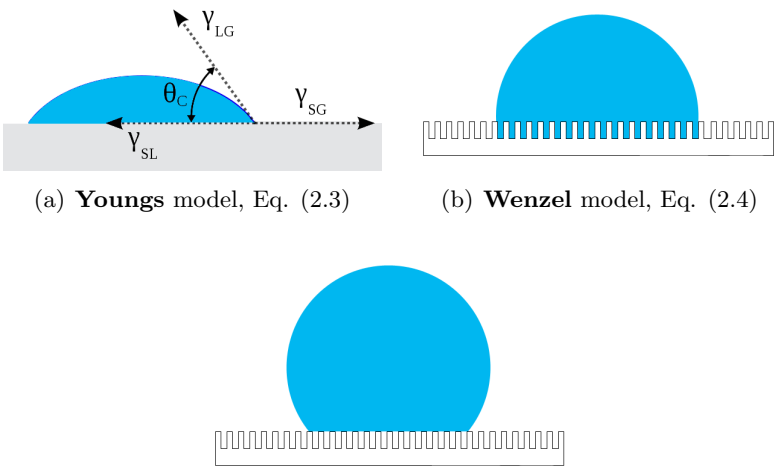

(a) **Youngs** model, Eq. (2.3)

(b) **Wenzel** model, Eq. (2.4)

(c) **Cassie-Baxter** model, Eq. (2.6)

Figure 2.1: Models of Young, Wenzel and Cassie-Baxter.

2.2.2 The Wenzel Equation

Wenzel determined that when a liquid is in intimate contact with a microstructure surface, $\boldsymbol{\theta}$ will be observed as $\boldsymbol{\theta}^*_W$. Due to the roughness, the angles on micro level does not reflect the angles observes on macro level. $\boldsymbol{\theta}^*$ is the apparent contact angle which corresponds to the minimum free energy state for the system. The Wenzel model [28] is described in figure 2.1(b).

$$cos\boldsymbol{\theta}^*_W = r\boldsymbol{\theta} \tag{2.4}$$

where r is the roughness ratio. Equation (2.4) displays that a surface with a microstructure amplifies the natural tendency of the surface. A hydrophobic surface, one that has an original contact angle greater than 90°, becomes more hydrophobic when microstructured. The new contact angle will become greater than the original. In the same way do also a hydrophilic ($\boldsymbol{\theta} < 90°$) surface become more hydrophilic. On a flat surface r equals 1, while a rough surface has $r > 1$, as in Eq. (2.2).

Ishino and Okumura states that the Wenzel model is valid only between $\boldsymbol{\theta}_C < \boldsymbol{\theta} < \pi/2$. If the contact angle is less than $\boldsymbol{\theta}_C$ a liquid film will form over the surface. The film will

smooth the surface and make the Wenzel model no longer valid. In this state Young's other relation yields [29].

$$\boldsymbol{\theta}^* = \boldsymbol{\varphi} cos\boldsymbol{\theta}_C + (1 - \boldsymbol{\varphi}) \tag{2.5}$$

where $\boldsymbol{\varphi}$ is the fraction of solid surface area wet by the liquid.

2.2.3 The Cassie-Baxter Equation

Cassie-Baxter proposed that if a liquid is suspended on the top of the microstructures, the $\boldsymbol{\theta}$ will be observes as $\boldsymbol{\theta}^*_{CB}$, equation (2.6), figure 2.1(c) views how they pictured a droplet on the surface [30].

$$\boldsymbol{\theta}^*_{CB} = \boldsymbol{\varphi}(cos\boldsymbol{\theta} + 1) - 1 \tag{2.6}$$

where $\boldsymbol{\varphi}$ is the fraction of solid surface area wet by the liquid.

Whether it is the Wenzel or Cassie-Baxter state that should exist can be predicted by calculating the new contact angle with both equations. The following inequality must be true for the Cassie-Baxter state to exist [31].

$$cos\boldsymbol{\theta}_C < \frac{\boldsymbol{\varphi} - 1}{r - \boldsymbol{\varphi}} \tag{2.7}$$

where $\boldsymbol{\theta}_C$ is the critical contact angle, $\boldsymbol{\varphi}$ is the fraction of solid/liquid interface where the drop is in contact with the surface and r is the solid roughness.

2.2.4 Contact Angle Hysteresis (CAH)

Contrary to Young's belief, a measurement of the contact angle $\boldsymbol{\theta}$ for a given solid-liquid-gas system will generally not be reproducible. Instead, if performing the same mesurements repeatedly, one will obtain a range of values in an interval $\triangle\boldsymbol{\theta}$. In other words there exists a range of stable contact angles for a given surface. This phenomenon is also seen if the liquid droplet is forced to move, for example by tilting the surface holding the droplet, see figure 2.2.

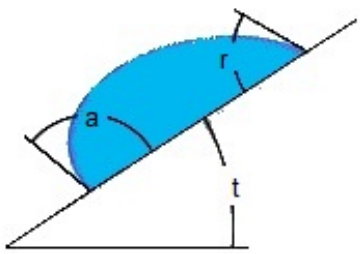

Figure 2.2: When the contact line of a droplet is forced to move, for example by tilting the surface, the droplet generally receeds and advances under different contact angles. t is the degree the surface is tilted, r denotes the receding angle and a denotes the advancing.

In experiments, it turns out that for a given surface, the liquid tend to advance and recede at fairly constant contact angles, the angle a and r at figure 2.2. It also turns out that the contact angle observed for a static droplet can lie anywhere between $\boldsymbol{\theta}_a$ and $\boldsymbol{\theta}_r$ [32]. note that tilting angle and CAH not necessary are the same. The interval $\triangle\boldsymbol{\theta}$ can thus be expressed as the difference $(\theta_a - \theta_r)$. The existence of this range of measurable contact angles is termed *contact angle hysteresis* (CAH).

$$\triangle\boldsymbol{\theta} = (\theta_a - \theta_r) \tag{2.8}$$

2.2.5 Criticism Against the Wenzel and Cassie-Baxter Models

Though the theories of Wenzel and Cassie-Baxter have been used to calculate the wetting abilities of surfaces for decades, later experiments show that they might not apply in all cases. Gao and McCarthy conclude in their paper that Wenzel's and Cassie-Baxter's equations are valid only to the extent that the structure of the contact area reflects the ground-state energies of the contact lines and the transition states between them [33]. All the data presented in the paper indicate that contact angle behavior is determined by interactions of the liquid and the solid at the three-phase contact line alone, and that the interfacial area within the contact perimeter is irrelevant. This supports the work of Bartell and Shepard [34] and questions the relevance of Wenzel and Cassie. That being said, Wenzel's and Cassie and Baxter's models will still be valid on uniform surfaces.

2.3 The Wetting Properties of Springtail

After the development of the first true SEM in the 1942 [35], it only took a 2 decades before Noble-Nesbitt [18] documented the general features of the springtail cuticle. He wrote "If a small drop of water is dropped on to the surface of *P. aquatica* it will not remain there, but it rolls off: the surface is unwettable." If a sample is forcibly submerged it quickly returns to the surface and is unwetted. This happens whether the arthropod is living or whether it is fixed in an aqueous fixative. This behaviour is confirmed in many papers, and in the latest by Helbig [22]. They explain how even tiny drops with diameters of only a few microns exhibited a spherical shape. Larger droplets occurred in a heterogeneous pattern typically observed with superhydrophobic surfaces and displays contact angles higher than 160°.

This was also confirmed by contact angle measurements released by Sandnes [36]. He performed contact angle measurements involving water droplets on nine different springtail species. The results displayed 7 out of 9 species with $\boldsymbol{\theta}_r > 160°$ and 6 out of 9 species with $\boldsymbol{\theta}_a > 160°$, thus providing two general findings. 1) Apparent contact angles are very high on springtail cuticles, and 2) with 1 exception, springtail cuticles display very low contact angle hysteresis.

3. Experimental Methodology

3.1 Instruments and Methods

The instruments used for the experimental part of this thesis were a Focused Ion Beam (FIB) and a Nanoindenter.

3.1.1 Focused Ion Beam (FIB)

The first instrument used was a Focused Ion Beam (FIB) with integrated Scanning Electron Microscopy (SEM). All SEM images presented were taken with FEI Company Helios Nanolab dual beam FP2067/32. The typical FIB instrument consists of a vacuum system, an Ga^+ liquid metal ion source (LMIS), ion column, stage, detectors, gas inlets, and a computer [37]. The combination of a SEM column and a FIB column forms a dual platform system that provides enhanced capabilities, see figure 3.1.

The Ga^+-ions will cause surface material to sputter, this damaging the sample. This is avoided when the electron beam is used. With the dual beam system, the user may locate and view the sample with the SEM without the risk of damage while the FIB provides the capability to mill material in the area imaged with the SEM [38].

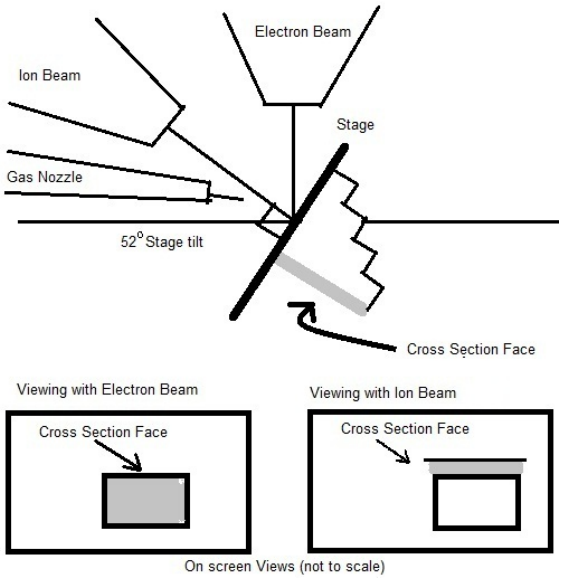

Figure 3.1: Dual-FIB beam column arrangement

The FIB can be used to mill into the bulk of a specimen. This is done by increasing the current of the ion beam to sputter away selected areas from the sample. This opens up a third dimension and explore the hidden internal micro structure [39].

When the FIB is started, the chamber is ventilated and the sample is placed on a sample holder. After evacuating the chamber, the stage moved to the working distance, approximately 4,1mm underneath the conductor. Then the eucentric point is found. The eucentric point is where beams from the FIB and SEM columns, which are placed at a 52 degree angle, converge [40], see figure 3.1. Finding the eucentric point on curved cuticles is more challenging than on typical flat samples.

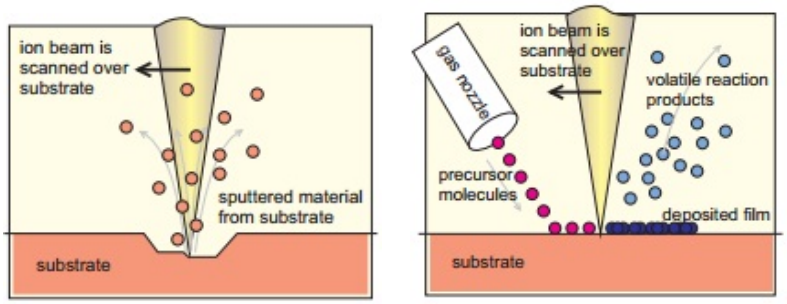

(a) Principle of FIB milling (b) Principle of FIB deposition

Figure 3.2: FIB milling and deposition [41]

A non-conducting sample, such as the springtail, will accumulate a net positive charge as a result of the impinging Ga^{+}-ions [38]. Charging the sample can cause drifting or errors in the displayed image [42]. The consequences are reduced accuracy of the images and the milling. To avoid this, a conductive coating is applied [43], explained in section 3.2.2.

To deposit platinum a gas delivery system is used together with the ion beam to produce site specific deposition of metals or insulators. The metals that can be deposited on commercially avaiable machines are platinum and tungsten [41]. The deposition process is illustrated in figure 3.2(b); the precursor gases are sprayed on the surface by a fine needle, where they adsorb. Then the ion beam decomposes the adsorbed precursor gases. The volatile reaction products are removed through the vacuum system, as the desired platinum is fixed on the surface as a thin film.

The cross-section imaging procedure is typically started by selecting a good area to examine the surface structures, as seen in figure 3.3(a). A thin layer (0,05 - 0,2 μm) of platinum is deposited on the selected area. To select this area, one has to view from the FIB, and thus some damage of the surface is unavoidable. Low current (9,7pA - 28pA)is used for the Pt deposition to avoid further damaging the surface, see figure 3.3(b). Then a thicker layer (2 - 3 μm) is deposited to further protect the surface from the damaging FIB source, see figure 3.3(c). This is done with the current as high as 0,92nA. The lower the current the more control you have over the thickness deployed, and do less damage of the surface, so care was taken as to not use too high current on the first layer. With higher current the damage of the FIB may also compensate for the metal deposited.

The milling process is illustrated in figure 3.2(a). The high ion beam current is physically sputtering the sample material at the desired area, as seen in figure 3.3(d). By selecting area and depth, a hole can be sputtered at desired place. To ease the milling of the slices we are interested in, two smaller gates are milled. This way the sputtered material has somewhere to go, and not damage the cross sections we are interest in. By looking with the SEM, a cross section of the sample can be viewed, see figure 3.3(e).

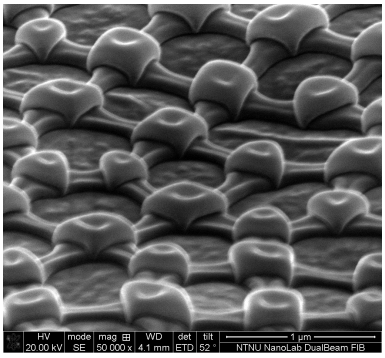

(a) Step 1: Select a good flat area to deposit material.

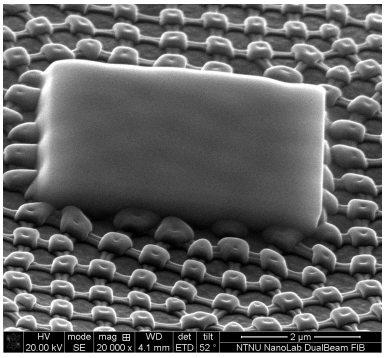

(b) Step 2: Deposit a thin layer with low current

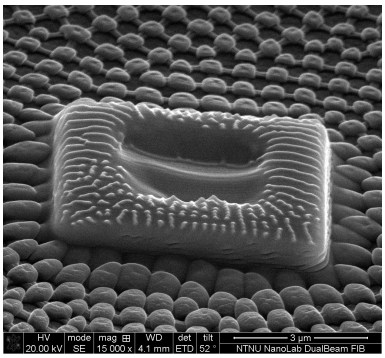

(c) Step 3. Deposit thicker layer with higher current

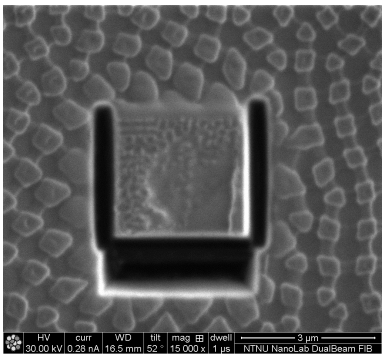

(d) Step 4: Select where to mill with the FIB. One bigger viewing area and 2 smaller slices at the sides.

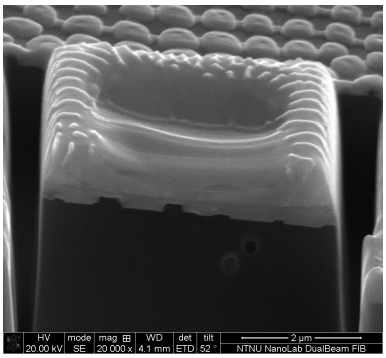

(e) Step 5: View cross section with SEM

Figure 3.3: Imaging cross sections with dual beam FIB/SEM

Slice and View

Milling and imaging can be done in a sequential manner, also called "slice and view". The FIB at NTNU Nanolab has a program that can repeat step four and five. The "slice and view" imaging procedure is started by selecting the area one wish to slice and view, drawn in green in figure 3.4. Then the slice thickness, usually between 3 and 6 nm, is selected. This is how much milling that is done between each SEM image, illustrated by the red line at figure 3.4. When the slice thickness and number of slices are chosen to correspond to the total width of the picture, a 3D picture of the selected area can be produced by image analytic software.

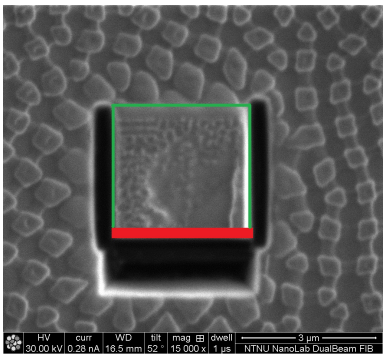

Figure 3.4: Select cross section, drawn in red, and the desired area to slice and view, drawn in green.

Note that this is a destructive way of generating a 3D image. Each time the FIB is milling away a cross section, that section will disappear, but not before a SEM image of the cross-section is taken.

3.1.2 Nanoindenter

The second instrument used in this thesis was a nanoindenter. A nanoindenter can produce 3D images of the surface of the sample when used as *in-situ Imaging*, or Nanoindenter-"Atomic Force Microscope" scanning, hereby called a NI-AFM scan. All indentations and NI-AFM scans were performed with the Hysitron TI 950 TriboIndenter.

The NI-AFM scanning procedure starts with placing the sample inside the nanoindenter. A microscope is used to select the test area and/or examine the effects of the test. In figure 3.6(b) we see how a springtail cuticle looks as viewed through the nanoindenter microscope. The indenter tip, that scans the sample, is driven by a piezoelectric actuator in the Z direction [44]. Three types of indenter tip geometries are in wide use: conospherical, with various angles and sharpnesses, Berkovich, three-sided pyramid with $142,35°$ included angle, or cube the corner with $90°$ included angle. An cube corner tip on fused quartz was used in this study. According to Hysitron this tip is suitable for *in-situ imaging*, or NI-AFM scanning [45]. In the Nanoindenter there is an magnetic table in an acoustically insulated cabinet to avoid vibrations or other disturbances during the testing [44]. The samples are mounted on a conductive sample holder to keep them fixed to the table.

The main use of a nanoindenter is to test materials of interest whose mechanical properties such as elastic modulus and hardness are unknown, this is called indenting. Usually the

principal goal of such testing is to obtain values for elastic modulus and hardness of the specimen material from experimental readings of indenter load and depth of penetration as the indenter tip is forced into the sample. The forces involved are usually in the range of millinewton range and measured with a resolution of a few nanonewtons [46].

Little research is found of others using the nanoindenter to perform NI-AFM scans, as most people mount an Atomic Force Microscope (AFM) inside the nanoindenter and use that to scan the surface. An AFM includes a tip mounted on a micro machined cantilever. As the tip scans a surface to be investigated, interatomic forces between the tip and the surface induce displacement of the tip. A laser beam is transmitted to and reflected from the cantilever for measuring the cantilever orientation. The reflected laser beam is detected with a position-sensitive detector [47].

The advantage of the NI-AFM over the AFM is that the user has much more control over the applied force. In this testing, forces as low as 0,1 μN, or in the range 0,3 - 0,7 μN was applied, as to not damage the sample. The scanned area, *scan size*, was usually between 3 and 6 μm. The speed of which the indenter scanned the area, *scan rate*, was as low as 0,2 Hz, but usually in the range of 0,4 - 0,8 Hz. The *scan size* and the *scan rate* form the tip velocity, which was always kept below 10 μm/s. The internal gain was 240.

With lower tip velocity, we can expect a better picture, as the indenter tip will have time to go into the smallest cracks of the surface. Though, some of the springtail cuticles have too big features, so the indenter tip will not reach the smaller details. This is exemplified in figure 3.5(a), as we see the result of a NI-AFM scan of *Onychiurus* versus a SEM image. It is speculated that the NI-AFM scan cant reach the area area between the secondary granules.

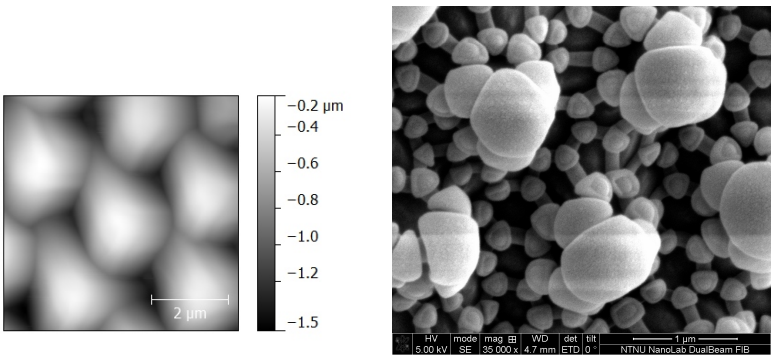

(a) NI-AFM scan

(b) SEM image at 35000x magnification

Figure 3.5: NI-AFM scan versus SEM image of *Onychiurus*, exemplifying that sometimes the resulting image cant view all the details

The different springtail cuticles are quite different to examine. Figure 3.6(b) to figure 3.6(a) views 4 different species of springtail as viewed through the microscope in the nanoindenter. The scan area are usually in the range of the inner blue circle visible at the pictures, but the indenter works best if there are not any movable objects in the way, for instance hairs.

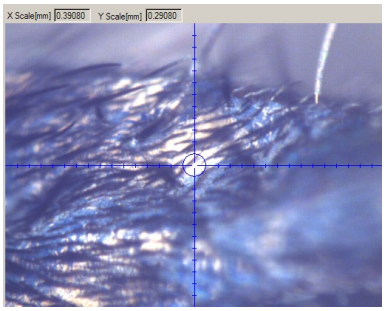

(a) *O. flavescens*(1) seen through nanoindenter microscope

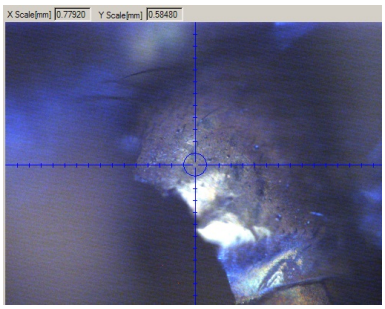

(b) *I. prasis*(2) seen through nanoindenter microscope

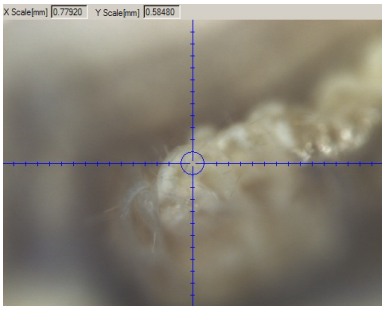

(c) *Onychiurus*(3) seen through nanoindenter microscope

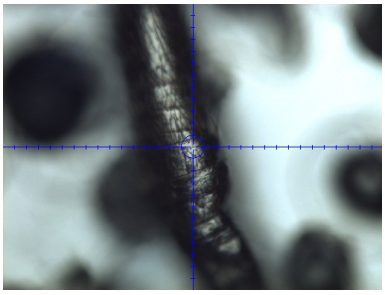

(d) *F. quadrioculata*(4) seen through nanoindenter microscope

Figure 3.6: Sample navigation in the nanoindenter

3.2 Sample Preparation

Different approaches are needed depending on whether the sample are to be used in the FIB or the nanoindenter. While indenting is performed in room temperature and ambient pressure, the FIB is working under vacuum.

3.2.1 Nanoindenter

The springtails were provided by Hans Petter Leinaas, professor in biology at the University in Oslo. The springtails were killed with chloroform vapour and immediately dried with a feeze-dry method. The freeze-dried samples were then mounted on stubs with carbon tape or silver glue. Great care was taken when placing the samples on the FIB stubs as the freeze-dried samples were very brittle. When performing a NI-AFM scan, we want the sample surface to be as natural as possible and show all the structures as close to when the arthropod was alive.

Some of the samples were also freshly killed springtails. They were killed and then directly mounted on the stubs and studied. This was also done with the samples that consisted of molted springtail skin. The species *H. viatica*(5) is routinely molting, or casting off its skin. The skins are neatly spread among the habitat and easily gathered. As fresh as possible molted skin were gathered and glued to stubs with silver glue.

3.2.2 FIB

As with the samples for the nanoindenter, the springtail species used as FIB samples were killed with chloroform and then freeze-dried. Then then freeze-dried samples were mounted on FIB stubs with carbon tape or silver glue. A thin layer of carbon was coated on the samples with a SEM Turbo Carbon Coater from Agar Scientific. The samples were mounted on a tilted, rotating stage. Typical settings for the carbon coating was 2 x 8 seconds with E = 4,8 kV. When finished with the carbon layer, the samples was sputter coated with platinum, either pure Pt or a 80/20 Pt/Pd alloy. The carbon coating layer improves the distribution and adhesion of the Pt coating. The thickness was in the range between 10 and 40 nm. The exact thickness is not important as more platinum is deposited after it is placed in the FIB.

3.3 Measurements

3.3.1 FIB

Cross-sections taken by the SEM can be manually measured, though some calculations are needed. The cross sections viewed by the operator is l', but the real heights are l, as in equation (3.1). This is due to the angle of the stage, as seen in figure 3.1.

$$l = l' * \frac{1}{sin52^\circ} \tag{3.1}$$

A cross section of the species *I. prasis*(2) can be viewed in figure 3.7. The image consists in large part of the platinum deposited on top of the structures. This is the grey/white part to protect the surface when milling. The black part is the actual cross section and the biological structure the springtail consists of. The line between the surface of the cuticle and the platinum deposited on top, is what is interesting. The rough surface of the cuticle is viewed as hills and valleys in the cross section. The red line is a thought extension of the base skin of the cuticle between the granules. A granule is clearly visible to the right, as the highest point away from a red line. The height of the granule will then be a perpendicular line from the red line, here drawn in yellow. Determining the height of the granule is now possible by extrapolating the distance of the length bar and with equation (3.1).

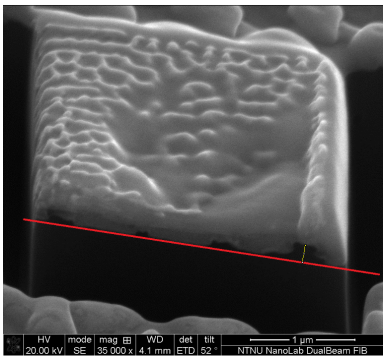

Figure 3.7: Measurement of granule heights on *I. prasis*(2)

3.3.2 NI-AFM Scans

The program Gwyddion was used to measure the heights on the images from the NI-AFM scans. Assumed the dark area between the granules are about the same level, the center between the granules were chosen as base. Then lines were drawn from the center to the granules and bridges between the granules, as seen in figure 3.8. Gwyddion then outputs $\triangle z$ as the biggest height difference along the line. Number 1 - 5 are height measurements of the granules and number 6 to 9 are measurements of the bridges between the granules. No measurement of the bridge between granule 4 an 5 was made since they are too close together.

Several granules and bridges on several scanned pictures makes the basis of calculating an average. Each image from the NI-AFM has been edited in some way to highlight the surface structures. Usually "level data by mean subtraction" and/or "level data to make facets point upward" in the image analysing program were applied. This do in little regard affect the height measurements, but do make the images look better, and the heights more emphasized.

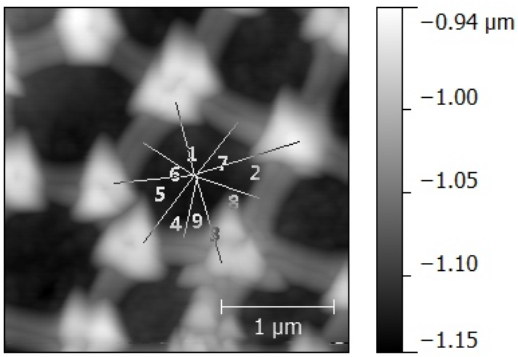

Figure 3.8: Height measurements of images from NI-AFM scans using Gwyddion

3.3.3 Indentations

Hardness (h) and reduced Young's modulus (E') were calculated from the load-displacement curves obtained by indentation. From the unloading part of the load-displacement curve, hardness and reduced modulus are obtained in the TriboView program [48]. The stiffness and contact area are calculated from standard tests, and the maximum force is extracted from the load-displacement curve.

Hardness is defined as the indentation load divided by the contact area of the indentation. This is the pressure that a material will support under load, and is calculated in Eq. (3.2).

$$h = \frac{P_{max}}{A(h_c)} \tag{3.2}$$

where h is *hardness*, $\boldsymbol{P}_{max}$ is *Maximum Force* and $\boldsymbol{A}(h_c)$ is *Contact Area*.

The reduced Young's modulus combines the modulus of the indenter and the specimen. The E' field is populated when the fit is executed and is calculated with in Eq. (3.3).

$$E_r = \frac{\sqrt{\pi}}{2\sqrt{A(h_c)}} * S \tag{3.3}$$

where $\boldsymbol{E}_r$ is *Reduced Modulus*, $\boldsymbol{A}(h_c)$ is *Contact Area* and $\mathbf{S}$ is *Stiffness*.

4. Results

First are SEM images of selected springtail cuticles presented, both overview picture and corresponding cross section. Then 3D images from the NI-AFM scans of the same species are presented. A few indents were performed to calculate the the reduced Young's modulus and the hardness of *F. quadrioculata*. Last the height data from the species are collected and calculated.

Table 4.1: Species numbering

Number	Species
1	*Orchesella flavescens*
2	*Isotomurus prasis*
3	*Onychiurus*
4	*Folsomia quadrioculata*
5	*Hypogastura viatica*

4.1 FIB Images

Surface images and cross sections of the species *O. flavescens*(1), fig. 4.1(a), *I. prasis*(2), fig. 4.2(a), *Onychiurus*(3), fig. 4.3(a), *F. quadrioculata*(4), fig. 4.4(a) and *H. viatica*(5), fig. 4.5(a). These were chosen as representatives of the different types of surface structures found on the springtail cuticle. All the cross sections have a thick layer of platinum deposited. The cross section of the actual arthropods are the black zone on the images.

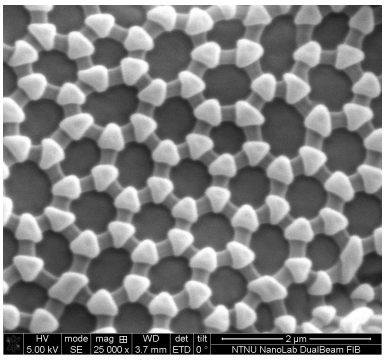

(a) Overview picture of *O. flavescens*(1) at 25 000x magnification

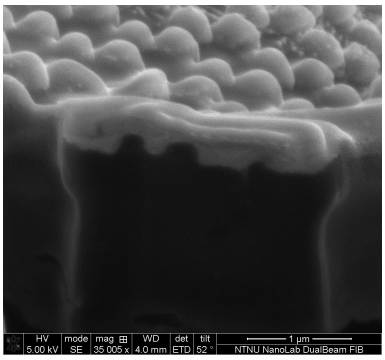

(b) Cross section of *O. flavescens*(1) at 35 005x magnification

Figure 4.1: SEM image of *O. flavescens*(1) pictured with SEM

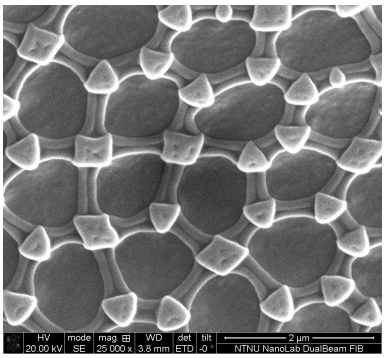

(a) Overview picture of *I. prasis*(2) at 25 000x magnification.

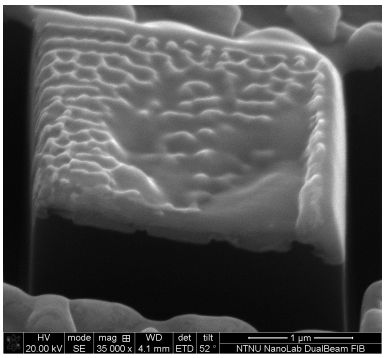

(b) Cross section of *I. prasis*(2) at 35 000x magnification

Figure 4.2: SEM images of *I. prasis*(2)

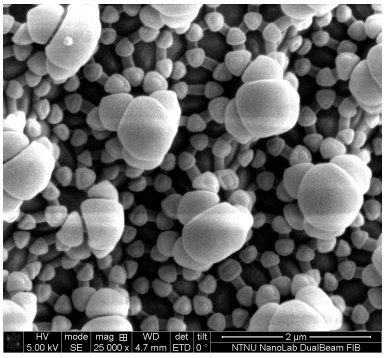

(a) Overview picture of *Onychiurus*(3) at 25 000x magnification

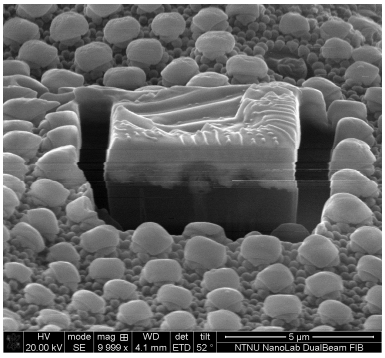

(b) Cross section of *Onychiurus*(3) at 9999x magnification

Figure 4.3: SEM image of *Onychiurus*(3)

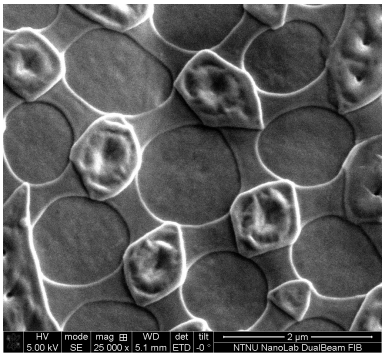

(a) Overview picture of *F. quadrioculata*(4) at 25 000x magnification

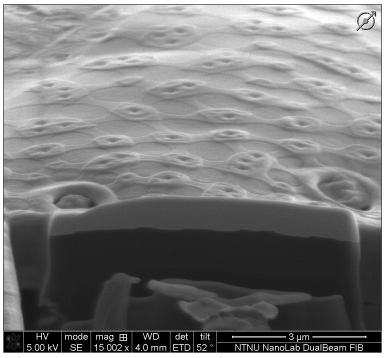

(b) Cross section of *F. quadrioculata*(4) at 15 002x magnification

Figure 4.4: SEM image of *F. quadrioculata*(4)

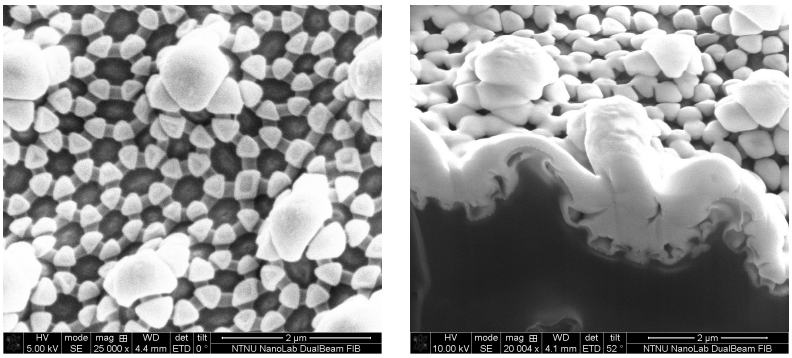

(a) Overview picture of *H. viatica*(5) at 25 000x magnification

(b) Cross section of *H. viatica*(5) at 20 004x magnification

Figure 4.5: SEM image of *H. viatica*(5)

4.1.1 3D Imaging

The NI-AFM scans produces a 3D image of the surface. Similar can be achieved by analysing hundreds of SEM pictures taken a few nm in between, the "slice and view" feature of the FIB. Figure 4.6 shows the species *H. viatica*(5) after analysing and merging all the SEM images from the "slice and view" method. The hexagonal structure of both the primary and secondary granules are still visible.

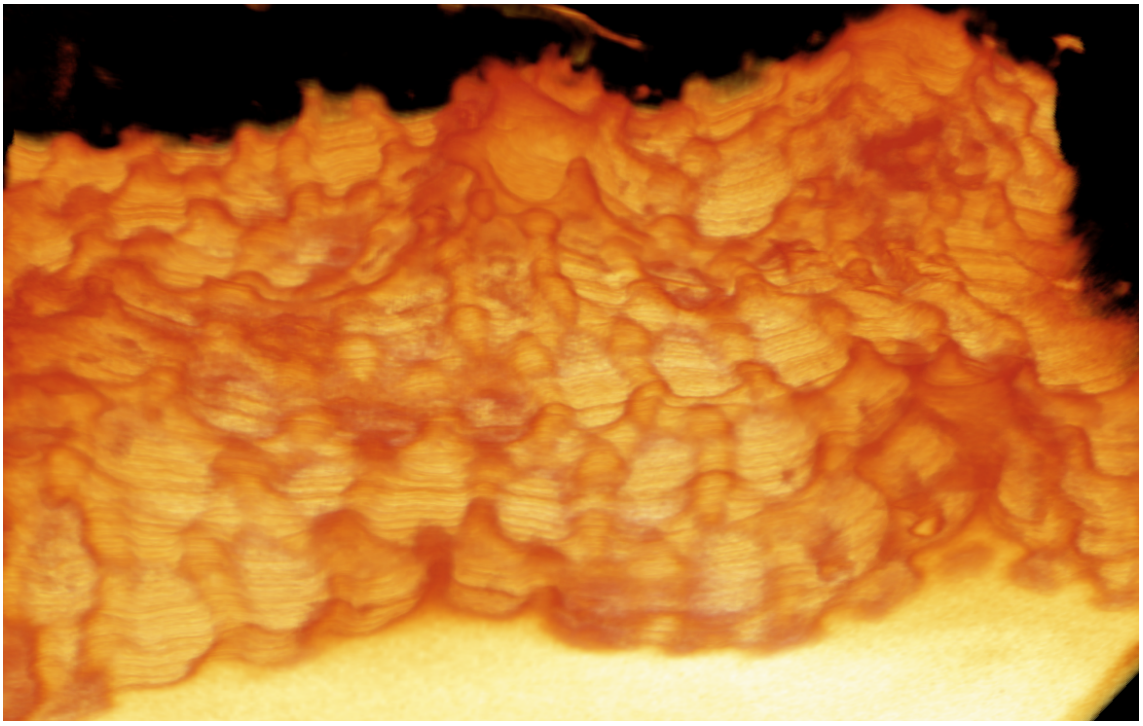

Figure 4.6: FIB Nanotomographic composite 3D image

4.2 NI-AFM Scans

In addition to cross-section of the cuticles, a nanoindenter was used to identify height differences on structures. Presented are images from NI-AFM scans. *H. viatica*(5) was deemed unscannable after several attempts.

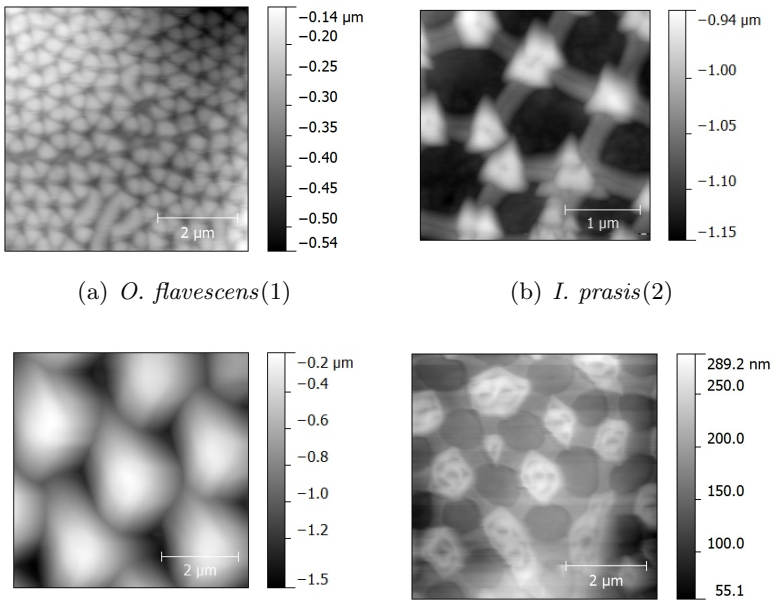

(a) *O. flavescens*(1)

(b) *I. prasis*(2)

(c) *Onychiurus*(3)

(d) *F. quadrioculata*(4)

Figure 4.7: Nanindenter scans of *I. prasis*, *Onychiurus*, *F. quadrioculata* and *O. flavescens*

4.2.1 Molting of Springtails

H. viatica(5) is one of the species of springtail that are molting, which is routinely casting off a part of its body, or skin. Their skins are neatly placed in their habitat without seeming to damage their own skin as they molt. Figure 4.8(a) shows the molted skin of *H. viaticas* versus SEM image of the freeze-dried arthropod in figure 4.8(b). As seen on the picture, the structures of the molted skin are quite similar as on the freeze-dried arthropod.

4.3 Indenting

Nanoindentations were performed on *F. quadrioculata*(4). Five indents on the granules, on the bridges between the granules and on the skin in between the granules, as seen in figure 4.9(c). Figure 4.9(a) shows the sample before the indents, and figure 4.9(b) after. All the samples did not display this good view of the surface after the indent, but here is clearly visible the mark of the cube corner tip on the skin between the granules.

Table 4.2 displays an average reduced Young's modulus E' of 0,145 GPa and a hardness of 0,065 GPa. This is the results of analysing, among others, the graph viewed in figure 4.10. The rest of the graphs and all calculations are in Appendix C.

The bridges are a little harder than the granule and the skin. There are a quite low standard deviation. This is because the sample size is small, but also shows that the

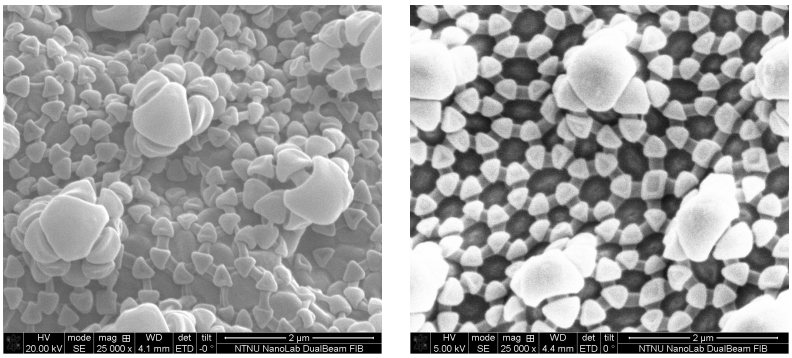

(a) The molted skin of *H. viaticas*. (b) The freeze-dried skin of *H. viaticas*.

Figure 4.8: *H. viaticas* molted versus freeze-dried

results of the different indents were close to each other.

Table 4.2: Indenting of *F. quadrioculata*

	Er(MPa)	H (MPa)	Standard deviation
Granule	145	66	4,5
Bridge	148	72	5,4
Skin	143	55	2,3
Average	145	65	

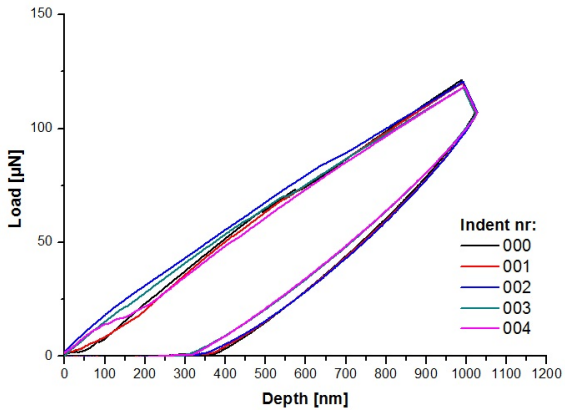

Figure 4.10: Indenting the granules of *F. quadrioculata*

4.4 Height Data

The height of the primary granules were measured and calculated from both the SEM images of the cross sections and the NI-AFM scans. The results of height measurements based on the NI-AFM scans can be viewed in table 4.3. The results of measurement on cross sections can be viewed in table 4.4.

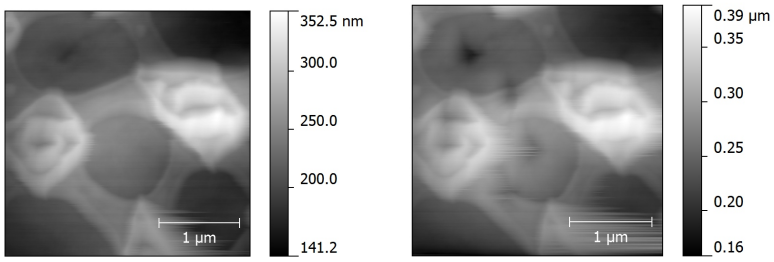

(a) Before the indents.

(b) After the indents

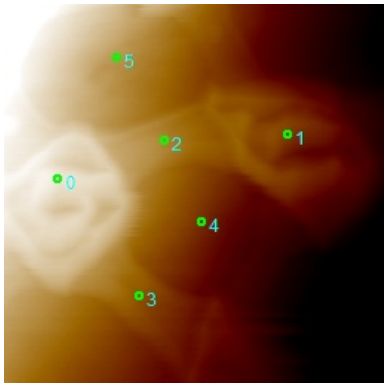

(c) Where indents were performed on *F. quadrioculata*

Figure 4.9: Nanindenting of *F. quadrioculata*

4.4.1 NI-AFM Scans

The height values are gathered from several NI-AFM scans of all the species. The resulting 3D image of the cuticle surface contains the height data. The measurements of the NI-AFM scans and corresponding images can be viewed in Appendix B, and the results is viewed in table 4.3. The species numbers are in the columns.

Measurable data of both the primary granules and the bridges were possible on *I. prasis*(2) and *F. quadrioculata*(4). Only the primary granules were possible to measure on *O. flavescens*(1) and only the secondary granules were possible to measure on *Onychiurus*(3). The number of datapoints varied from 19 to 38 and were dependent on how good and how many scans there existed on each species.

4.4.2 FIB

The height data are on most species collected from only one good SEM picture of the cross section, but several measurements have been made since one picture can contain several granules. Sometimes several measurements were made on one granule as well. Further calculations and SEM images of the cross sections are in Appendix A. The species numbers are in the columns.

Measurable data of both the primary granules and the bridges were possible on *I. prasis*(2) and *F. quadrioculata*(4), as from the NI-AFM scans. Only the primary granules were possible to measure on *O. flavescens*(1) and only the secondary granules were possible to

Table 4.3: Nanoindenter height values [nm]

	Species #	1	2	3	4
H(primary)	Average	115	199		72
	Min	95	141		31
	Max	155	280		106
	St. Dev.	14	50		21
h(bridge)	Average		84		17
	Min		35		2
	Max		145		39
	St. Dev.		32		11
H(secundary)	Average			1042	
	Min			917	
	Max			1207	
	St. Dev.			90	
# of results		38	25	19	22

measure on *Onychiurus*(3). *O. flavescens*(1), *I. prasis*(2) and *Onychiurus*(3) had only a few good pictures, and thus few datapoints. *F. quadrioculata*(4) had more good pictures, and thus more good datapoints (# of results).

Table 4.4: Cross section height values [nm]

	Species #	1	2	3	4
H(primary)	Average	203	169		92
	Min	186	165		76
	Max	215	173		113
	St. Dev	11	4		13
h(bridge)	Average		52		53
	Min		36		38
	Max		70		66
	St. Dev		11		9
H(secundary)	Average			937	
	Min			912	
	Max			964	
	St. Dev			20	
# of results		5	6	5	20

5. Discussion

Height measurements of the granules on the cuticle of five different species of springtails were performed. There existed great variations of the surface structure among the different species, as was expected [18] [19] [20] [21]. *I. prasis* and *F. quadrioculata* had very low primary granule heights and no secondary granules. The cuticle of *H. viatica* and *Onychiurus* had huge secondary granules, in addition to the primary ones.

The height measurements were done with two different methods. Method one was to take SEM pictures of the cross section of the species. Care was taken as to not damage the surface in this procedure, but there is still a chance the surface was damaged by the ion beam. To analyse the cross section images, a line had to be drawn as a baseline. Then a perpendicular line was drawn. This was manually done, as one had to select and see where the surface was on each image. As Kristin Fjellvang [49] also noticed, it might be difficult to determine where the line between the granule and platinum exactly is drawn. On the less good SEM images there was a gray area. This was not a problem highly noticed. The samples with the lowest heights also seemed the hardest to analyse. This might be due to the fact that there was very small heights, and difficult to measure exactly.

The second method was to scan the cuticles of the springtails with a nanoindenter, perform a NI-AFM scan. This was a more direct method, as less hampering with the samples were needed. The NI-AFM scans were performed with very low force as to damage the surface as little as possible, and with slow speed to scan as much of the surface as possible. Nevertheless, there were narrow openings where the indenter tip was too big to fit in, and so the whole surface could not be imaged. The tip only scratched the surface between two hills without displaying the real valley. This was clearly the effect on the NI-AFM scan of *Onychiurus*, figure 4.7(c), and to some extent on the NI-AFM scan of *O. flavescens*, figure 4.7(a), both in section 4.2.

In both methods, the height data of the granules were affected of where the measurement was taken. This is why several measurements were made and an average drawn. As seen in the results, more measurements could be done. In addition, the amount of good images, and thus possible measurements were affected by the specie of springtail. No good NI-AFM scans could be performed on *H. viatica*(5), and only a few on *Onychiurus*(3). The best results, statistically speaking was the nanoindenter results of *O. flavescens*(1), with 38 datapoints and a standard deviation of only 14nm.

With two different methods generating the same height data, are they comparable? They were acquired on the same species, but it was different samples on both tests. In addition, there were different parts of the arthropod analysed on each method. Since these are biological creatures, no guarantee was given that each of its granules had the same size.

Seen in table 4.3 and 4.4 are quite noticeable differences of the height data, but also some equalities. *Onychiurus*(3) and *I. prasis*(2) both had almost the same height measured by both methods. On *O. flavescens*(1) the height measured on the NI-AFM scan images are half of what are measured by the cross section SEM images from the FIB.

It seems to be a problem performing good NI-AFM scans on certain species. One hypothesis was that the molted skin of the species might be better. No good scan of *H. viatica* was possible, and chance was that this species also was molting. No more testing was done after one working day without viable results.

The 3D images from the NI-AFM scans contain height data of the surface analysed. "slice and view"-images should contain height values as well. The only problem was that each of the SEM pictures the "slice and view" 3D image contains was without data bar, no reference could be extracted. In addition, the process of taking all the images was time consuming. Due to overcharging and drifting, many times the SEM images after a "slice and view" process was too bad to generate a 3D picture from. This adds up to being a time consuming process that produces no real scientific data, but only a good looking 3D picture of the surface to look at. With more experience, understanding and attention during the generating of these pictures there might be possible to get the height values.

The indents on *F. quadrioculata* resulted in a calculated reduced Young's modulus E'= 0,145 GPa and hardness h = 0,065 GPa. In comparison, Aluminium [50] has $E' \approx 80$GPa and $h \approx 0,8$GPa. On lobsters [51], the values are at $E' \approx 15$GPa , and hardness $h \approx 0,37$GPa. These samples are both much harder than the springtails, as expected. Frankie [52] has performed indents on several soft tissues, such as cartilage, and softer materials such as wood. He found E' values of such materials to be in the range around 0,5GPa, but also as low as 0,2GPa. The hardness h of these materials was in the range of 0,0005 to 0,001 GPa. These results are more comparable to *F. quadrioculata*. It seems the E' values measured are in the lower region of comparable materials, but the h value are higher. This adds value to the knowledge that springtails has a relatively hard cuticle [22].

Kaufman [53] reminds us that the accuracy of mechanical properties from nanoindentations depends on the accuracy of the displacement measurement used to calculate these properties. Tests starting below the sample surface, such as between the granules, can cause an overestimation of elastic modulus. One thing is certain, and that is the value of the indents compared to each other. Which means that it was proven that the granules and bridges between the granules on *F. quadrioculata* are a little harder than the skin between them.

As the lotus leaf consists of papillose epidermal cells covered in self-assembled nanocrystalline wax tubules [4], we have seen that the springtail has a similar form of two stage hierarchy, with the higher granules and the lower bridges between them. As Patankar [13] produced double (or triple) roughness structures on pillars to mimic the lotus leaf, the future would be to do something similar based on the springtail design. Now that we have the proper tools and methods to characterize the exact size of the structures on the springtail cuticle, it should not be that hard to apply some well known methods to construct something similar. Intricate surface designs are vulnerable to damage and defects. In recent years there has been much research on lubricants that improve wettability [54]. This method depends on a lubricating liquid that impregnates the surface.

6. Conclusion

Two different methods of surface characterization have been discussed. The first method was analysing of SEM images of cross section taken with the FIB. The other method was analysing the images from a NI-AFM scanning.

Depending on the species, one of the two methods was preferred. *H. viatica* could not even be scanned by the NI-AFM. *I. prasis* and *F. quadrioculata* had small features, easily scanned by the NI-AFM. *Onychiurus* had big secondary granules and it is questioned if the indenter tip even touched the surface between the granules. *O. flavescens* actually seemed quite difficult to get good results from with both methods. The conclusion is that springtail cuticles with small surface structures, such as *I. prasis* and *F. quadrioculata*, gets best results from the NI-AFM and are harder to analyse by the FIB scans. The species with bigger structures as *H. viatica* and *Onychiurus* or with lots of hairs as *O. flavescens* are best characterized in a FIB.

"Slice and view" 3D images could be useful if the surface was to be replicated, especially if the NI-AFM is not able to scan the surface at all.

The NI-AFM scanning of the molted springtail skin was unsuccessful. FIB is as alternative method to the NI-AFM. It is recommendation is to use the FIB for the species that are unscannable.

The characterization of the mechanical properties of the springtail confirmed some of what we already know. The granules and bridges between the granules are harder than the skin between them. Nanoindentation of soft materials is a field increasing in scope. More material testing of the cuticles of springtails are reccomended.

New methods of producing superhydrophobic surfaces emerge, such as impregnated nanotextured surfaces. Surface textures with intricate designs and morphologies are vulnerable to defects. The conclusion must be to further investigate the intricate designs. This way we may produce superhydrophobic materials that are more resistant and do not need the coating to stay superhydrophobic. Springtails could be a vital part in this field due to their characteristic surface structures.

7. Further Work

Recommended future work is the continuation of the characterization of the surface structures. To get a good probability of the size of the granules, more testing are needed. The recommended method in this thesis can be applied on the selected species. In addition are several pictures attached, more data can be extracted from those.

The continuation of mechanical testing could determine the real strength of the springtails. Are the granules harder on all the species? Are there huge differences on different species? When mimicking the structure of the springtail cuticle is the goal, knowing the strength and weaknesses of the biological sample could be beneficial. Fabrication of man-made surfaces mimicking the springtail cuticle presents exciting possibilities.

References

[1] Bharat Bushan and Yong Chae Jung. Natural and biomimetic artificial surfaces for superhydrophobicity, self-cleaning, low adhesion and drag reduction. *Progress in Materials Science*, 3:1–9, 2010.

[2] W. Barthlott and C. Neinhuis. Purity of the sacred lotus, or escape from contamination in biological surfaces. *Planta*, 202:1–8, 1997.

[3] Abraham Marmur. The lotus effect: Superhydrophobicity and metastability. *Department of Chemical Engineering, Israel Institute of Technology*, 20:3517–3519, 2004.

[4] Luping Xu Hang Ju Qi Ouyang Dapeng Yu Manhui Sun, Chunxiong Luo and Yong Chen. Artificial lotus leaf by nanocasting. *Langmuir*, 21:8978–8981, 2005.

[5] Xuefeng Gao and Lei Jiang. Biophysics: Water-repellent legs of water striders. *Nature*, 432:36, 2004.

[6] W. R. Hansen and K. Autumn. Evidence for self-cleaning in gecko state. *Proc Natl Acad Sci USA*, 102:385–389, 2005.

[7] M. Bruse D. W. Bechert and W. Hage. Experiments with tree-dimensional riblets as an idealized model of shark skin. *Experiments in Fluids*, 28:403–412, 2000.

[8] S.J. Wilson and M.C. Hutley. The optical properties of moth eye antireflection surfaces. *Optica Acta: International Journal of Optics*, 29:7:993–1009, 1982.

[9] Na2jojon. Drop connection angel. *http://en.wikipedia.org/wiki/File:DropConnectionAngel.jpg*, 2007.

[10] Bjørn Christian Tørrissen. Gecko foot on glass. *http://en.wikipedia.org/wiki/File:GeckoFootOnGlass.JPG*, 2009.

[11] Albert Kok. Carcharhinus amblyrhynchos wake. *http://en.wikipedia.org/wiki/File:CarcharhinusAmblyrhynchosWake.jpg*, 2007.

[12] Joaquim Alves Gaspar. Drop connection angel. *http://en.wikipedia.org/wiki/File:EmperorGumMoth.jpg*, 2008.

[13] Neelesh A. Patankar. mimiching the lotus effect: Influens of double roughness structures and slender pillars. *Department of Mechanical Engineering, Northwestern University*, 20:8209–8213, 2004.

[14] Timothy Sullivan and Fiona Regan. The characterization, replication and testing of dermal denticles of scyliorhinus canicula for physical mechanisms of biofouling prevention. *IOP publishing, Bioinsp. Biomim.*, 6:1–10, 2011.

[15] P.A. Shields C. Liu D.W.E. Allsopp W.N. Wang Q. Chen, G. Hubbard and S. Abbott. Broadband moth-eye antireflection coatings fabricated by low-cost nanoimprinting. *Applied physics letters*, 94:1, 2009.

[16] Tom Mueller. Biomimetics: Design by nature. *National Geographic Magazine*, 1:2, 2008.

[17] Hans Petter Leinaas Christian Thaulow Thor Christian Hobæl, Kristian Greger Leinan. Surface nanoengineering inspired by evolution. *BiNanoSchi*, 1:9–12, 2011.

[18] J. Noble-Nesbitt. Transpiration in podura aquatica l. and the wetting properties of its cuticle. *Department of Zoology, University of Cambrudge*, 40:689–691, 1963.

[19] Cedric Gillott et al. *Entomology.* Springer The Netherlands, 2005.

[20] PE King, PJA Pugh, MR Fordy, N Love, and SA Wheeler. A comparison of some environmental adaptations of the littoral collembolans anuridella marina (willem) and anurida maritima (guérin). *Journal of Natural History*, 24(3):673–688, 1990.

[21] Helen Ghiradella and William Radigan. Collembolan cuticle: wax layer and anti-wetting properties. *J. Insect Physiol*, 20:301–306, 1974.

[22] Ralf Helbig, Julia Nickerl, Christoph Neinhuis, and Carsten Werner. Smart skin patterns protect springtails. *PloS one*, 6(9):e25105, 2011.

[23] IP Hayward, IL Singer, and LE Seitzman. Effect of roughness on the friction of diamond on cvd diamond coatings. *Wear*, 157(2):215–227, 1992.

[24] Gwidon W Stachowiak and Andrew W Batchelor. *Engineering tribology.* Butterworth-Heinemann, 2005.

[25] Robert N Wenzel. Surface roughness and contact angle. *The Journal of Physical Chemistry*, 53(9):1466–1467, 1949.

[26] J. Bikerman. Method of measuring contact angles. *Analytic Chemistry*, 13(6):443–444, 1941.

[27] Thomas Young. An essay on the cohesion of fluids. *Sec. R.S*, 95(1):1–5, 1804.

[28] Robert N. Wenzel. Resistance of solid surfaces to wetting by water. *Mellon Institute of Industrial Research*, 28:989–991, 1936.

[29] C. Ishino and K. Okumura. Wetting transitions on textured hydrophilic surfaces. *Eur. Phys. J. E*, 25:415–424, 2008.

[30] A. B. D. Cassie and S. Baxter. Wettability of porous surfaces. *RSC Publishing*, 40:546–547, 1944.

[31] David Quere. non-sticking drops. *Institute of Physicks publishing*, 68:2510–2512, 2005.

[32] Lichao Gao and Thomas J McCarthy. Wetting 101. *Langmuir*, 25(24):14105–14115, 2009.

[33] Lichao Gao and Thomas J. McCarthy. How wenzel and cassie were wrong. *Polymer Science and Enineering Department, University of Massachusetts*, 23:2765, 2007.

[34] F. E. Bartell and J. W. Shepard. Surface roughness as related to hystersis of contact angles. *The Journal of Physical Chemistry*, 57:455, 1953.

[35] A Bogner, P-H Jouneau, Gilbert Thollet, D Basset, and Catherine Gauthier. A history of scanning electron microscopy developments: towards "wet-stem" imaging. *Micron*, 38(4):390–401, 2007.

[36] Runar Sandnes. Wetting properties of springtail cuticles: A quantitative analysis. *Norwegian University of Science and Technology*, pages 35 – 40, 2012.

[37] Jon Orloff, Lynwood Swanson, and Mark William Utlaut. *High resolution focused ion beams: FIB and its applications: The physics of liquid metal ion sources and ion optics and their application to focused ion beam technology.* Springer, 2003.

[38] Lucille A Giannuzzi et al. *Introduction to focused ion beams: instrumentation, theory, techniques and practice.* Springer, 2004.

[39] DJ Stokes, F Morrissey, and BH Lich. A new approach to studying biological and soft materials using focused ion beam scanning electron microscopy (fib sem). In *Journal of Physics: Conference Series*, volume 26, page 50. IOP Publishing, 2006.

[40] Miroslava Schaffer, Julian Wagner, Bernhard Schaffer, Mario Schmied, and Hans Mulders. Automated three-dimensional x-ray analysis using a dual-beam fib. *Ultramicroscopy*, 107(8):587–597, 2007.

[41] Steve Reyntjens and Robert Puers. A review of focused ion beam applications in microsystem technology. *IOP Science*, 287(11):287–300, 2001.

[42] DJ Stokes, T Vystavel, and F Morrissey. Focused ion beam (fib) milling of electrically insulating specimens using simultaneous primary electron and ion beam irradiation. *Journal of Physics D: Applied Physics*, 40(3):874, 2007.

[43] BW Kempshall, LA Giannuzzi, BI Prenitzer, FA Stevie, and SX Da. Comparative evaluation of protective coatings and focused ion beam chemical vapor deposition processes. *Journal of Vacuum Science & Technology B: Microelectronics and Nanometer Structures*, 20(1):286–290, 2002.

[44] Weidian Shen, Jian Sun, Jhiqiang Liu, Wenjing Mao, J David Nordstrom, Paul D Ziemer, and Frank N Jones. Methods for studying the mechanical and tribological properties of hard and soft coatings with a nano-indenter. *Journal of Coatings Technology and Research*, 1(2):117–125, 2004.

[45] Hysitron Corporation. Hysitron nanomechanical testing probe selection guide. *http://www.hysitron.com/products/options/indenter-tips*, 2010.

[46] Anthony C. Fischer-Cripps. *Nanoindentation.* Springer, 2004.

[47] Nabil M Amer and Gerhard Meyer. Atomic force microscopy, 1992. US Patent 5,144,833.

[48] Hysitron Incorporated. Ti 950 triboindenter user manual. Revision 9.2.1211:112–113, 2011.

[49] Kristing Fjellvang. Lessons from nature, the wetting of springtail cuticles. *Norwegian University of Science and Technology*, pages 43 – 64, 2012.

[50] C.G. Kangb H.H. Kima, S.H. Choa. Evaluation of microstructure and mechanical properties by using nano/micro-indentation and nanoscratch during aging treatment of rheo-forged al 6061 alloy. 485:272–281, 2008.

[51] H. Fabritius C. Sachs and D. Raabea. Hardness and elastic properties of dehydrated cuticle from the lobster homarus americanus obtained by nanoindentationy. 21(2):1987–1995, 2006.

[52] Oliver Franke, Mathias Göken, and Andrea M Hodge. The nanoindentation of soft tissue: current and developing approaches. *JOM Journal of the Minerals, Metals and Materials Society*, 60(6):49–53, 2008.

[53] Jessica D Kaufman and Catherine M Klapperich. Surface detection errors cause overestimation of the modulus in nanoindentation on soft materials. *Journal of the Mechanical Behavior of Biomedical Materials*, 2(4):312–317, 2009.

[54] Sushant Anand, Adam T Paxson, Rajeev Dhiman, J David Smith, and Kripa K Varanasi. Enhanced condensation on lubricant-impregnated nanotextured surfaces. *ACS nano*, 6(11):10122–10129, 2012.

[55] Wilhelm Barthlott and Christoph Neinhuis. Purity of the sacred lotus, or escape from contamination in biological surfaces. *Planta*, 202(1):1–8, 1997.

A. FIB measurements

Attached are all the cross section images the height data are collected from. They are all corrected according to the given equation.

$$l = l' * \frac{1}{\boldsymbol{s}in52^{\circ}} \tag{A.1}$$

A repetition of the table from section 4 could be in order since all species in the Appendix are numbered.

Table A.1: Species numbering

Number	Species
1	*Orchesella flavescens*
2	*Isotomurus prasis*
3	*Onychiurus*
4	*Folsomia quadrioculata*
5	*Hypogastura viatica*

A.1 Species 1

Table A.2: Species 1

	H (primary)				
Picture	Picture	corrected		Average	203
1	201	204		min	186
	212	215		max	215
	183	186		St. Dev.	11
	201	204			
	206	208			

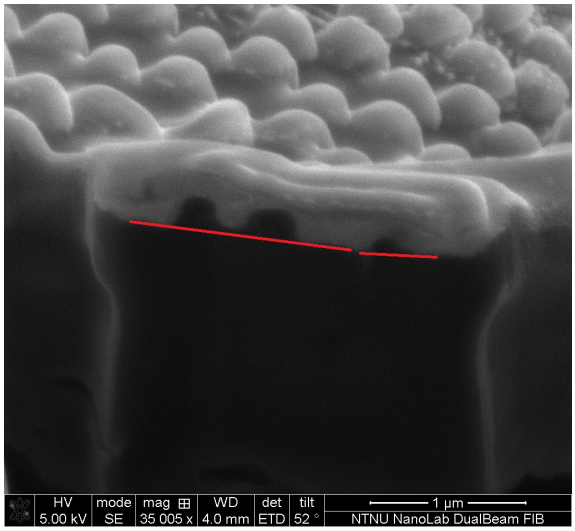

Figure A.1: Species 1

A.2 Species 2

Table A.3: Species 2

	h(bridge)		H(granule)				h	H
Picture	picture	corrected	picture	corrected		Average	52	169
1	49	50	171	173		min	36	165
	49	50	165	167		max	70	173
	69	70	163	165		St. Dev	11	4
	36	36						
	51	51						
	54	55						

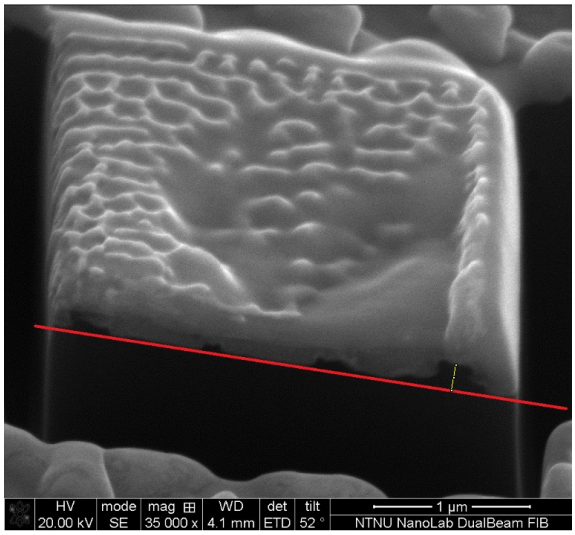

Figure A.2: Species 2

A.3 Species 3

Table A.4: Species 3

	H(secundary)			H(secundary)
Picture 1	picture	corrected	Average	937
			min	912
	900	912	max	964
	951	964	St. Dev	20
	916	928		
	919	931		
	934	947		

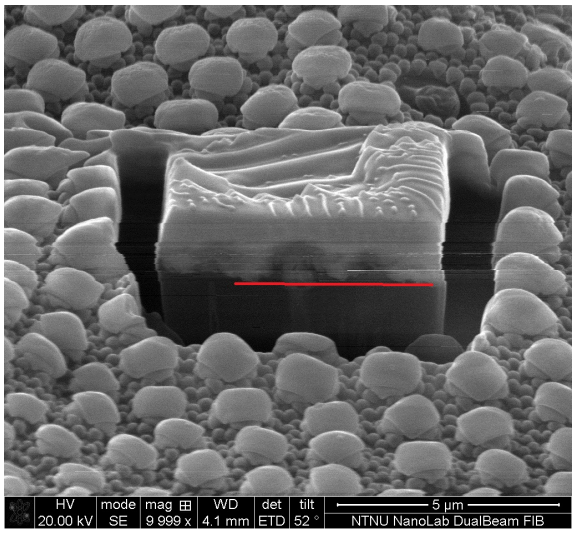

Figure A.3: Species 3

Table A.5: Species 4

	h (bridge)		H (granule)			corrected	h (bridge)	H (granule)
Picture	picture	corrected	picture	corrected		Average	53	92
1	47	47	93	95		min	38	76
	47	47	75	76		max	66	113
	57	57	100	101		St. Dev	9	13
	37	38	90	91				
	47	47	78	79				
2	65	66	111	113				
	56	57	100	101				
	65	66	78	79				
	47	47						
	57	58						
3	55	56						
	45	46						

A.4 Species 4

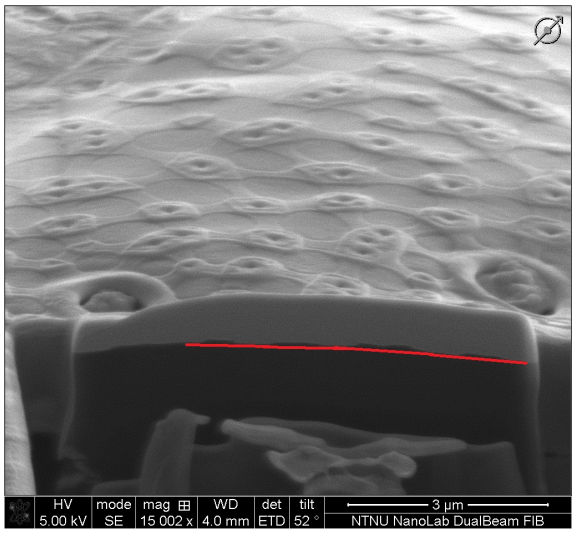

(a) Picture 1

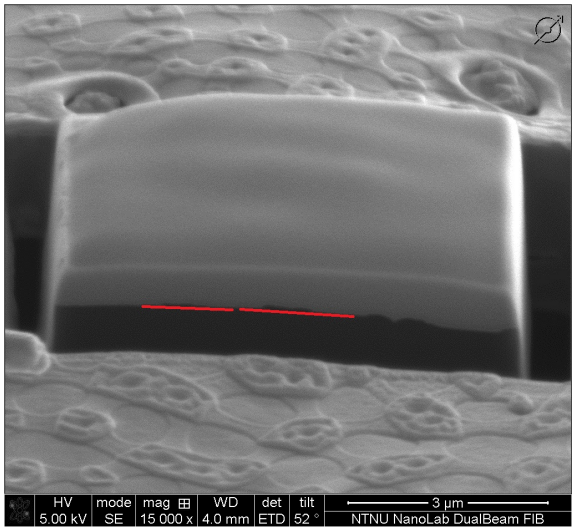

(b) Picture 2

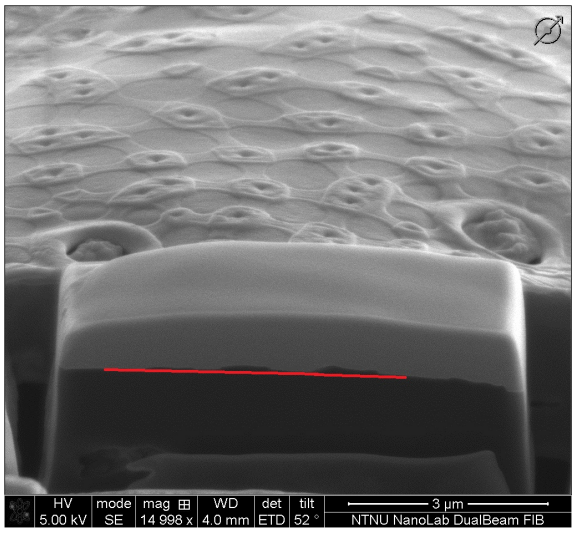

(c) Picture 3

Figure A.4: Species 4

B. Measurement of NI-AFM scans

Attached are all the measurements with the including images from the NI-AFM scans.

B.1 Species 1

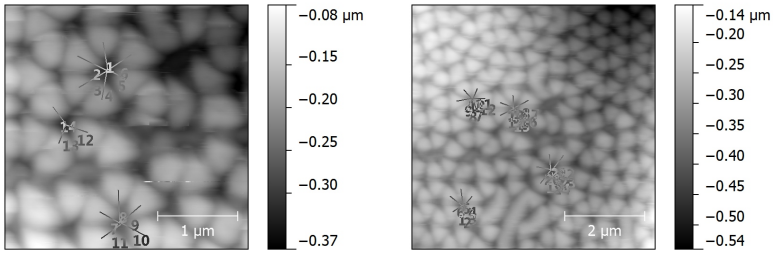

(a) Picture 1 (b) Picture 2

Figure B.1: Species 1

Table B.1: Species 1

	H (primary)	#		H (primary)
Picture 1	108	1	Average	115
	125	2	min	95
	121	3	max	155
	122	4	St. Dev	14
	103	5		
	102	6		
	111	7		
	104	8		
	101	9		
	130	10		
	138	11		
	138	12		
	155	13		
	139	14		
Picture 2	123	1		
	103	2		
	106	3		
	111	4		
	105	5		
	125	6		
	95	7		
	95	8		
	113	9		
	113	10		
	105	11		
	98	12		
	134	13		
	111	14		
	97	15		
	97	16		
	118	17		
	127	18		
	127	19		
	113	20		
	120	21		
	117	22		
	113	23		
	127	34		

Table B.2: # are the measurement number

Table B.3: Species 2

	H (granule) [nm]	#	h (bridge) [nm]	#		H(granule)	h(bridge)
Picture 1	254	1	102	6	Average	199	84
	264	2	107	7	Min	141	35
	255	3	67	8	Max	280	145
	280	4	115	9	St. Dev	50	32
	225	5	143	10			
Picture 2	264	1	89	6			
	245	2	126	7			
	263	3	111	8			
	267	4	126	9			
	249	5	145	10			
Picture 3	169	1	73	6			
	156	2	48	7			
	161	3	47	8			
	192	4	76	9			
	154	5	50	10			
Picture 4	165	1	80	6			
	160	2	91	7			
	143	3	35	8			
	141	4	49	9			
	178	5					
Picture 5	167	1	54	6			
	178	2	74	7			
	144	3	70	8			
	159	4	64	9			
	154	5					

Table B.4: # are the measurement number

B.2 Species 2

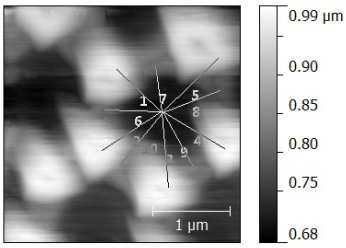

(a) Picture 1

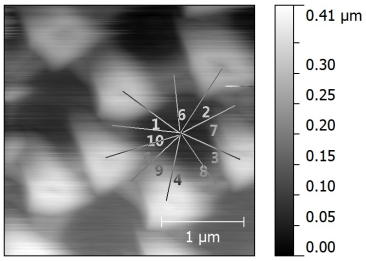

(b) Picture 2

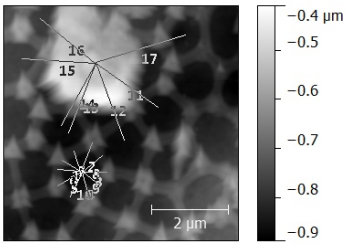

(c) Picture 3

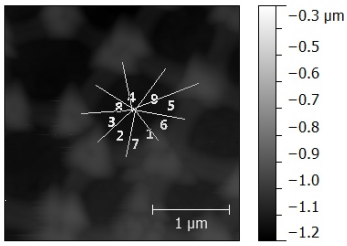

(d) Picture 4

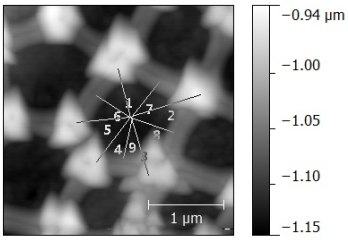

(e) Picture 5

Figure B.2: Species 2

B.3 Species 3

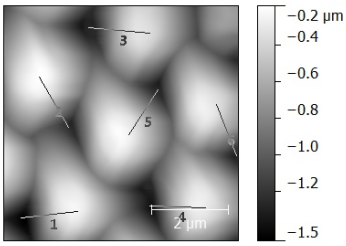

(a) Picture 1

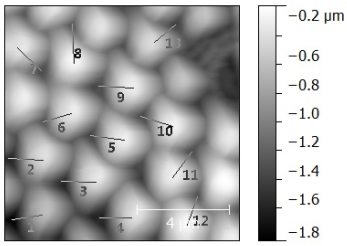

(b) Picture 2

Figure B.3: Species 3

Table B.5: Species 3

	H (secundary)	#		
Picture 1	1207	1	Average	1042
	1042	2	Min	917
	917	3	Max	1207
	1082	4	St. Dev	90
	1013	5		
	926	6		
Picture 2	1177	1		
	1130	2		
	1150	3		
	1164	4		
	1067	5		
	946	6		
	934	7		
	991	8		
	1018	9		
	1030	10		
	1018	11		
	1034	12		
	947	13		

Table B.6: # are the measurement number

B.4 Species 4

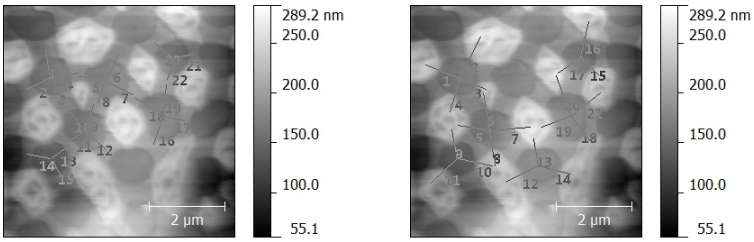

(a) Measurements on the bridges (b) Measurements on the granules

Figure B.4: Species 4

Table B.7: Species 4

	H(granule)	#	h(bridge)		G(granule)	h(bridge)
Picture 1	77	1	7	Average	72	17
	101	2	8	min	31	2
	63	3	8	max	106	39
	65	4	20	St. Dev	21	11
	62	5	7			
	70	6	8			
	101	7	25			
	72	8	12			
	84	9	22			
	91	10	10			
	59	11	10			
	46	12	39			
	75	13	36			
	34	14	10			
	83	15	18			
	63	16	26			
	106	17	4			
	31	18	13			
	75	19	19			
	94	20	29			
	51	21	2			
		22	31			

Table B.8: # are the measurement number

C. Nanoindenting

Attached are the graphs of the indentations done of specie 4. Including an overview picture of where the indentations were done and the resulting calculations done by the TriboView program.

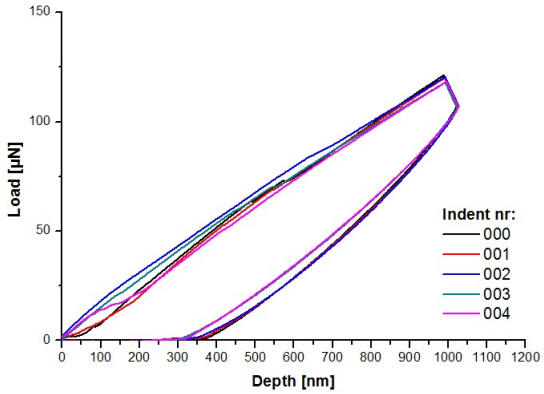

(a) Indenting on the granules

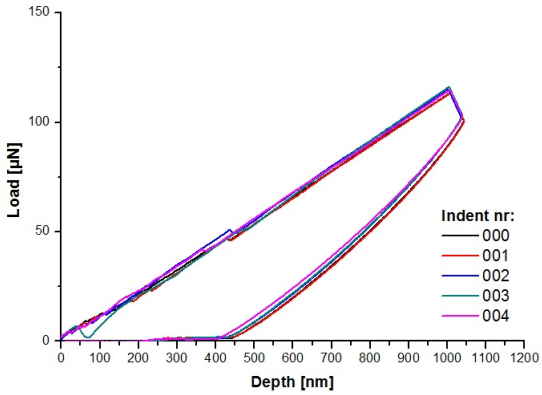

(b) Indenting in the middle between the granules

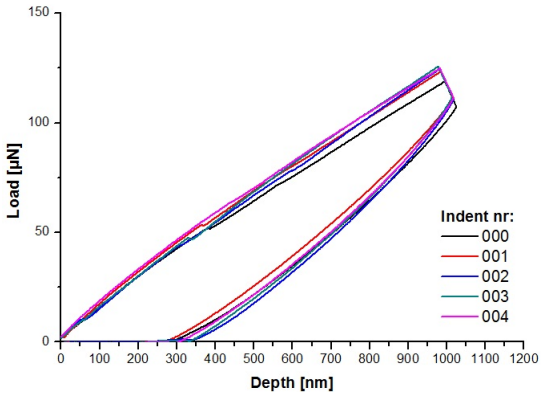

(c) Indenting on the bridges between the granules

Figure C.1: Nanoindenting graphs

Number of Data Points = 5															
Granule	contact desplacement						Reduced modulus	Hardness							
File	hc(nm)	Pmax(µN)	S(µN/nm)	A(nm^2)	hmax(nm)	heff(nm)	Er(GPa)	H(GPa)	A	hf(nm)	m	X(mm)	Y(mm)	Drift(nm/s)	Er(Mpa)
Art4_000.hys	625,803175	106,195402	0,194923	1516405,48	1022,03763	1034,40815	0,140246	0,070031	0,005616	232,158838	1,47254	-111,857974	-105,07988	0,010618	140,246
Art4_001.hys	620,907077	106,6596	0,191142	1496643,73	1026,34974	1039,41584	0,138431	0,071266	0,007002	235,948431	1,439876	-111,85615	-105,079527	-0,256676	138,431
Ledd4_001.hy	665,443266	107,757419	0,217703	1680988,31	1023,14642	1036,67406	0,148771	0,064104	0,004487	283,066329	1,522519	-111,846545	-105,150207	-0,38332	148,771
Ledd4_002.hy	668,196832	106,705606	0,215976	1692724,19	1025,20676	1038,74418	0,147078	0,063038	0,00331	267,293052	1,561442	-111,847934	-105,149454	-0,23919	147,078
Ledd4_003.hy	677,773562	107,126332	0,221989	1733847,63	1027,06688	1039,70445	0,149369	0,061785	0,001739	243,044575	1,650854	-111,847087	-105,15143	-0,28052	149,369
						Average	0,144779	0,0660448	0,0044308	252,302245	1,5294462	-111,851138	-105,1221	-0,2298176	144,779
						St. Dev	0,00454169	0,00384978	0,00181774	19,6471967	0,07358357	0,00489128	0,0346222	0,13019387	4,54169039
Number of Data Points = 5															
Bridge															
File	hc(nm)	Pmax(µN)	S(µN/nm)	A(nm^2)	hmax(nm)	heff(nm)	Er(GPa)	H(GPa)	A	hf(nm)	m	X(mm)	Y(mm)	Drift(nm/s)	Er (Mpa)
Art4_002.hys	619,139667	107,353222	0,192578	1489540,67	1024,61405	1037,23014	0,139802	0,072071	0,006354	226,954104	1,45353	-111,857127	-105,079574	-0,251755	139,802
Art4_003.hys	595,860529	111,386054	0,19299	1397498,66	1014,86501	1028,73012	0,144642	0,079704	0,007321	201,414125	1,433427	-111,857327	-105,08081	-0,283676	144,642
Ledd4_005.hy	655,537145	111,0658	0,221241	1639093,56	1017,71369	1032,04605	0,153109	0,067761	0,00336	248,180026	1,561449	-111,846263	-105,152277	-0,313228	153,109
Ledd4_007.hy	645,621383	112,002281	0,219744	1597668,68	1013,07842	1027,8922	0,154031	0,070104	0,003025	226,07062	1,573142	-111,844498	-105,150865	-0,270557	154,031
Indent_005.h	633,096357	111,527074	0,209969	1546073,35	1017,20591	1031,46591	0,149615	0,072136	0,003493	210,533498	1,545548	-111,849403	-105,146651	-0,354344	149,615
						Average	0,1482398	0,0723552	0,0047106	222,630475	1,5134192	-111,850924	-105,122035	-0,294712	148,2398
						St. Dev	0,00535311	0,0040077	0,00176991	15,9986142	0,05812298	0,00538159	0,03421734	0,03591484	5,35310965
Number of Data Points = 5															
Between															
File	hc(nm)	Pmax(µN)	S(µN/nm)	A(nm^2)	hmax(nm)	heff(nm)	Er(GPa)	H(GPa)	A	hf(nm)	m	X(mm)	Y(mm)	Drift(nm/s)	Er (Mpa)
Ledd4_008.hy	711,107705	100,77448	0,219466	1880703,99	1042,37102	1055,49238	0,141789	0,053583	0,004201	349,500884	1,537506	-111,848875	-105,150536	-0,528701	141,789
Ledd4_009.hy	714,757573	100,543749	0,220968	1897134,48	1043,31292	1056,01872	0,14214	0,052998	0,003798	349,650788	1,552406	-111,847392	-105,15063	-0,296028	142,14
Ledd4_010.hy	704,193721	102,417242	0,223546	1849769,28	1034,88011	1047,80516	0,145627	0,055368	0,003678	334,161602	1,557668	-111,845981	-105,151524	-0,184343	145,627
Ledd4_011.hy	703,948383	103,249836	0,222904	1848676,15	1038,83982	1051,35072	0,145252	0,055851	0,003481	327,020207	1,563743	-111,848922	-105,15263	-0,432222	145,252
Indent_008.h	683,788599	102,353142	0,209024	1759920,47	1039,08477	1051,04219	0,1396	0,058158	0,005314	318,658169	1,495664	-111,849309	-105,145992	-0,352073	139,6
						Average	0,1428816	0,0551916	0,0040944	335,79833	1,5413974	-111,848096	-105,150262	-0,3586734	142,8816
						St. Dev	0,002265774	0,00182565	0,00065365	12,2733045	0,02446195	0,00124333	0,00226466	0,11719887	2,26577409

Figure C.2:

D. Additional pictures

Attached are more pictures that i find interesting and beautiful to watch. Would be a waste to not be viewed by others than my self.

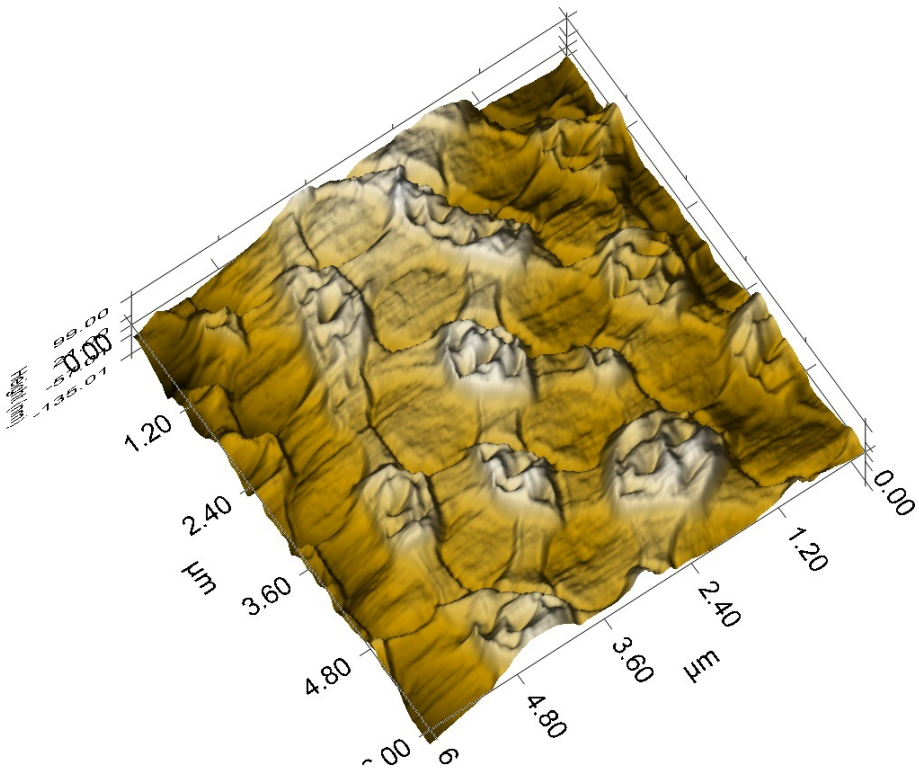

Figure D.1: NI-AFM scan of *F. quadrioculata*(4), viewed in 3D

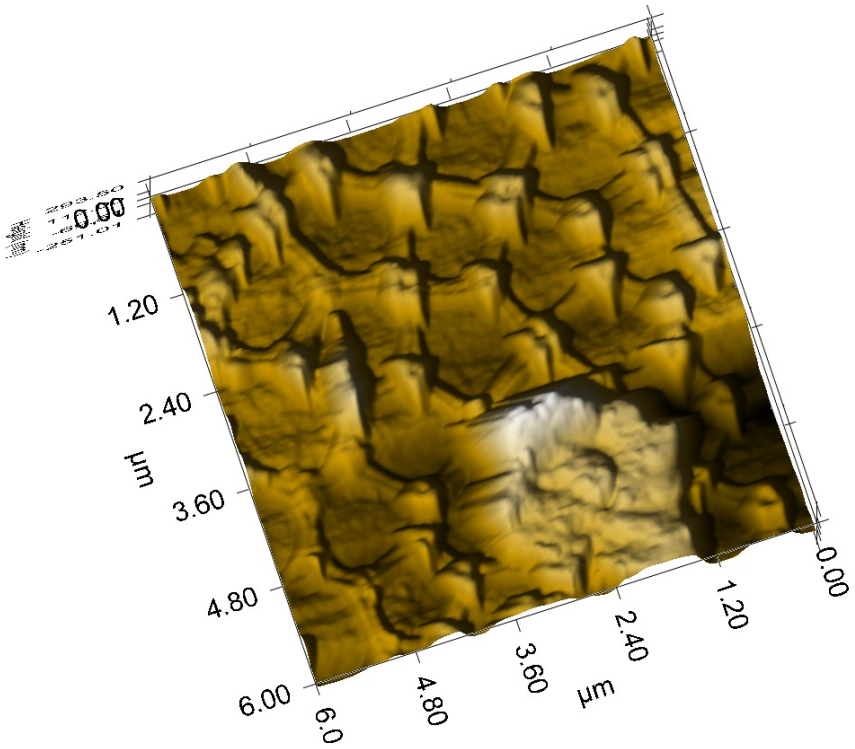

Figure D.2: NI-AFM scan of *Isotomurus prasis*(2), viewed in 3D

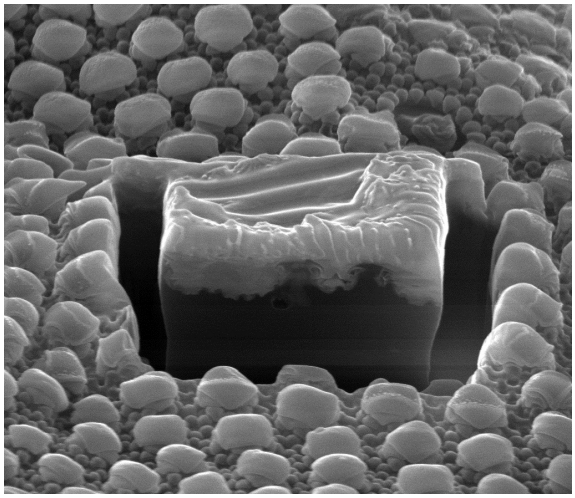

(a) Picture 1

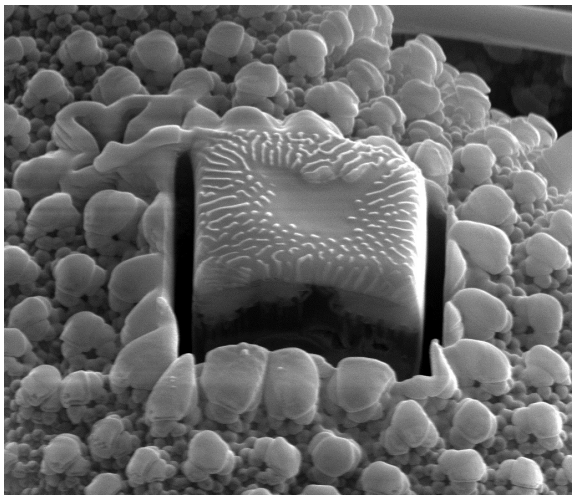

(b) Picture 2

Figure D.3: Cross sections of *Onychiurus*(3)